Take 5: Interpretable Image Classification with a Handful of Features

Thomas Norrenbrock **Marco Rudolph** **Bodo Rosenhahn**
Institute for Information Processing (tnt)
L3S - Leibniz Universität Hannover, Germany
{norrenbr, rudolph, rosenhahn}@tnt.uni-hannover.de

Abstract

Deep Neural Networks use thousands of mostly incomprehensible features to identify a single class, a decision no human can follow. We propose an interpretable sparse and low dimensional final decision layer in a deep neural network with measurable aspects of interpretability and demonstrate it on fine-grained image classification. We argue that a human can only understand the decision of a machine learning model, if the features are interpretable and only very few of them are used for a single decision. For that matter, the final layer has to be sparse and - to make interpreting the features feasible - low dimensional. We call a model with a Sparse Low-Dimensional Decision "*SLDD-Model*". We show that a *SLDD-Model* is easier to interpret locally and globally than a dense high-dimensional decision layer while being able to maintain competitive accuracy. Additionally, we propose a loss function that improves a model's feature diversity and accuracy. Our more interpretable *SLDD-Model* only uses 5 out of just 50 features per class, while maintaining 97 % to 100 % of the accuracy on four common benchmark datasets compared to the baseline model with 2048 features.

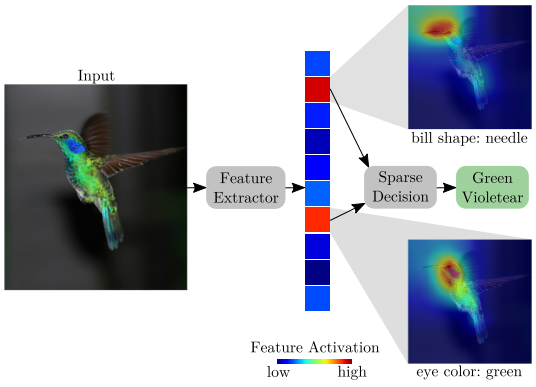

Figure 1: Local explanation by our *SLDD-Model*: The two features used for the predicted class, emerged without additional supervision, are aligned with human interpretable attributes and localized (described in App. D) adequately.

1 Introduction

Understanding the decision of a deep learning model is becoming more and more important. Especially for safety-critical applications such as the medical domain or autonomous driving, it is often either legally (Bibal et al., 2021) or by the practitioners required to be able to trust the decision and evaluate its reasoning (Molnar, 2020). Due to the high dimensionality of images, most previous work on interpretable models for computer vision combines the deep features computed by a deep neural network with a method that is considered interpretable, such as a prototype based decision

2022 Trustworthy and Socially Responsible Machine Learning (TSRML 2022) co-located with NeurIPS 2022.

tree (Nauta et al., 2021). While approaches for measuring the interpretability without humans exist for conventional machine learning algorithms (Islam et al., 2020), they are missing for methods including deep neural networks. In this work, we propose a novel sparse and low-dimensional *SLDD-Model* which offers measurable aspects of interpretability. The key aspect is a heavily reduced number of features, out of which only very few are considered per class. Humans can only consider 7 ± 2 aspects at once (Miller, 1956) and could therefore follow a decision that uses that many features. To be intelligible for all humans, we aim for an average of 5 features per class.
Having a reduced number of features makes it feasible to investigate every single feature and understand its meaning: We are able to align several of the learned features with human concepts post-hoc. The combination of reduced features and sparsity therefore increases both global *How does the model behave?* and local interpretability *Why did the model make this decision?*, demonstrated in Figure 1. Our proposed method generates the *SLDD-Model* by utilizing *glm-saga (Wong et al., 2021)* to compute a sparse linear classifier for selected features, which we then finetune to the sparse structure. We apply feature selection instead of a transformation to reduce the computational load and preserve the original semantics of the features, which can improve interpretability (Tao et al., 2015), especially if a more interpretable model like *B-cos Networks* (Böhle et al., 2022) is used. Additionally, we propose a novel loss function for more diverse features, which is especially relevant when one class depends on very few features, since using more redundant features limits the total information available for the decision.

Our main **contributions** are as follows:

- We present a pipeline that ensures a model with increased global and local interpretability which identifies a single class with just few, *e.g.* 5, features of its low-dimensional representation. We call the resulting model *SLDD-Model*.
- Our novel feature diversity loss ensures diverse features. This increases the accuracy for the extremely sparse case.
- We demonstrate the competitive performance of our proposed method on four common benchmark datasets in the domain of fine-grained image classification as well as ImageNet-1K (Russakovsky et al., 2015), and show that several learned features for algorithmic decision-making can be directly connected to attributes humans use.

2 Related Work

2.1 Fine-Grained Image Classification

Fine-grained image classification describes the problem of differentiating similar classes from one another. It is more challenging compared to conventional image recognition tasks (Lin et al., 2015) since the differences between classes are much smaller. To tackle this difficulty, several adaptions to the common image classification approach have been applied. They usually involve learning more discriminative features by adding a term to the loss function (Chang et al., 2020; Liang et al., 2020; Zheng et al., 2020), introducing hierarchy to the architecture (Chou et al., 2022) or using expensive expert knowledge (Chen et al., 2018; Chang et al., 2021). Chang et al. (2020) divide the features into groups, s. t. every group is assigned to exactly one class. While training, an additional loss increases the activations of features for samples of their assigned class and reduces the overlap of feature maps in each group. Liang et al. (2020) tried to create class-specific filters by inducing sparsity in the features. Both (Chang et al., 2020) and (Liang et al., 2020) optimize for class-specific filters, which are neither suitable for the low-dimensional case when the number of classes exceeds the number of features nor interpretable, since it is unclear if the feature is already detecting the class rather than a lower level feature. The *Feature Redundancy Loss* (Zheng et al., 2020) (FRL) enforces the K most used features to be localized differently by reducing the normalized inner product between their feature maps. This adds a hyperparameter and does not optimize all features at once.

2.2 Interpretable Machine Learning

Interpretable machine learning is a broad term and can refer to both models that are interpretable by design, and post-hoc methods that try to understand what the model has learned. Furthermore, interpretability can be classified as the interpretability of a single instance (local) or the entire model (global) (Molnar, 2020).
In this work, we present methods making models more interpretable by design but also utilize post-hoc

methods to offer local and global interpretability. Common local post-hoc methods are saliency maps like Grad-CAM (Selvaraju et al., 2017) that aim to show what part of the input image is relevant for the prediction. While they can be helpful, they have to be cautiously interpreted, as they do not show many desired properties one would expect from an explanation like shift invariance (Kindermans et al., 2019) or only producing reasonable explanations, when the model is working as intended (Adebayo et al., 2018). Another way of obtaining saliency maps is based on masking the input image and measuring the impact on the output (Zeiler and Fergus, 2014; Fong and Vedaldi, 2017; Jain et al., 2022).

As a global post-hoc method, *Elude* (Ramaswamy et al., 2022) generates an explanation for a model by mimicking its behavior with a sparse model. This model uses additional attributes and main directions of the remaining feature space of the model as input. Instead of explaining a model, we directly train the more interpretable model in this work. Another line of research tries to align learned representations with human understandable concepts from an additional labeled dataset (Kim et al., 2018; Bau et al., 2017; McGrath et al., 2021), increasing the global interpretability of the model. While algorithms may aim to make the models decision more interpretable (*e.g.* applications of fuzzy models in game AI (Dockhorn and Kruse, 2021)), to the best of our knowledge, measuring the interpretability of a deep neural network is an open task, as previous work focuses on measuring the quality of explanations of black boxes (Rokade and Alluri, 2021) or on conventional machine learning algorithms (Islam et al., 2020), where increased interpretability is measured when model complexity is reduced, *e.g.* via the number of operations (Yang et al., 2017; Friedler et al., 2019; Rüping et al., 2006) or number of features (Rüping et al., 2006). The sparsity and low-dimensionality of our proposed *SLDD-Model* is motivated by these findings. Due to the limitations of post-hoc methods in explaining a deep neural network, models that are more interpretable by design are becoming more relevant. Prototype based models like *ProtoTree* (Nauta et al., 2021), *ProtoPNet* (Chen et al., 2019), *ProtoPShare* (Rymarczyk et al., 2021) and *ProtoPool* (Rymarczyk et al., 2022) combine a deep feature extractor with a more interpretable model by using the similarities to learned prototypes as input to the linear model or decision tree. While they achieve competitive performance on fine-grained image classification, Kim et al. (2021) and Hoffmann et al. (2021) indicate a gap between the perceived similarities of humans and prototype based models. *Concept bottleneck models* (*CBM*) (Koh et al., 2020) first predict concepts annotated in the dataset and then use a simple model to predict the target class from the concepts. *CBM-AUC* (Sawada and Nakamura, 2022) extended *CBM* by allowing unsupervised concepts to influence the decision. *PCBM* (Yuksekgonul et al., 2022) created a post-hoc *CBM* using *TCAV* (Kim et al., 2018) to compress high-dimensional learned features into a concept bottleneck. Margeloiu et al. (2021) and *Elude* (Ramaswamy et al., 2022) both suggest that training the *CBM* end-to-end leads to the encoding of additional information next to the concepts, which reduces the interpretability. In contrast to *CBM*, our proposed method does not require additional labels for training and leads to a very sparse decision process. While their features are generally more aligned with the given concepts, they also need to be analyzed thoroughly.

2.2.1 *Glm-saga*

Wong et al. (2021) developed *glm-saga*, a method to efficiently fit a heavily regularized sparse layer to the computed features of a backbone feature extractor by combining the path algorithm of Friedman et al. (2010) with advancements in variance reduced gradient methods by Gazagnadou et al. (2019). They showed that human understanding is more aligned with the decision process of the sparse model and sparsely shared features can be more easily aligned with human concepts. Additionally, they reached levels of sparsity that network wide sparsity methods do not obtain in the final layer with competitive accuracy (Gale et al., 2019). For precomputed and normalized features, *glm-saga* computes a series of n sparse linear classifiers

$$P = [(\boldsymbol{W}_1^{\text{sparse}}, \boldsymbol{b}_1), (\boldsymbol{W}_2^{\text{sparse}}, \boldsymbol{b}_2), \ldots, (\boldsymbol{W}_n^{\text{sparse}}, \boldsymbol{b}_n)], \tag{1}$$

where the sparsity of $\boldsymbol{W}_i^{\text{sparse}}$ is decreasing with i. This series is called *regularization path*. Each of the models minimizes the elastic net loss

$$\mathcal{L} = \mathcal{L}_{\text{target}} + \lambda R(\boldsymbol{W}) \qquad R(\boldsymbol{W}) = (1-\alpha)\frac{1}{2}\|\boldsymbol{W}\|_F + \alpha\|\boldsymbol{W}\|_{1,1} \tag{2}$$

with the initial optimization goal $\mathcal{L}_{\text{target}}$, in our case the cross-entropy loss, and regularization strength λ, which decreases along the path. The regularization function R($\boldsymbol{W}$) with weighting factor $\alpha \in [0, 1]$ is known as Elastic Net (Zou and Hastie, 2005). *Glm-saga* optimizes the problem iteratively, clipping entries in $\boldsymbol{W}$ with an absolute value below a threshold after each step, to ensure real sparsity. For reference, the pseudocode for *glm-saga* is included in Appendix C. Since their

aim is understanding the neural network, they fit the sparse layer to fixed features and do not finetune the features to the sparse layer, which requires different optimization strategies than dense networks (Tessera et al., 2021). In this work, we utilize *glm-saga* to create a more interpretable model with competitive accuracy by applying it on selected features with higher diversity and finetuning the features afterwards. This leads to improved accuracy and enables a higher sparsity which, combined with the reduced number of features,increases interpretability.

3 Method

3.1 Problem Formulation

We apply the proposed *SLDD-Model* to the domain of fine-grained image classification. We consider the problem of classifying an image $\boldsymbol{I} \in \mathbb{R}^{3\times w\times h}$ of width w and height h into one class $c \in \{c_1, c_2, \ldots, c_{n_c}\}$ using a trainable deep neural network Φ. This neural network extracts the feature maps $\boldsymbol{M} \in \mathbb{R}^{n_f\times w_M\times h_M}$ and aggregates them into the feature vector $\boldsymbol{f} \in \mathbb{R}^{n_f}$. Then it applies the trainable neural network C to obtain the final output $\boldsymbol{y} \in \mathbb{R}^{n_c}$ as $\boldsymbol{y} = C(\boldsymbol{f})$.

3.2 *SLDD-Model*

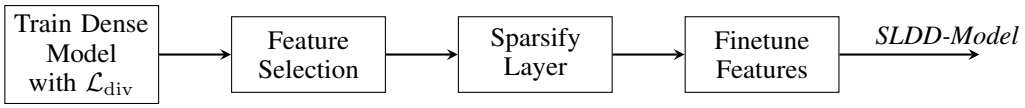

Figure 2: Overview of our proposed pipeline to construct a *SLDD-Model*

We propose a flexible, generally applicable method for generating a more locally and globally interpretable model with no need for additional labels and an adjustable tradeoff between interpretability and accuracy. We make the decision process more interpretable by only using n_f^* features with $n_f^* \ll n_f$ and using an interpretable classifier C. At the core of an interpretable classifier C lies a linear layer $\boldsymbol{y} = \boldsymbol{W}\boldsymbol{f} + \boldsymbol{b}$ with the weight matrix $\boldsymbol{W} \in \mathbb{R}^{n_c\times n_f^*}$ and bias $\boldsymbol{b} \in \mathbb{R}^{n_c}$. In order for it to be interpretable, $\boldsymbol{W}$ has to be very sparse, meaning the number of non-zero entries n_w has to be very low. Miller (1956) showed that humans can handle 7 ± 2 cognitive aspects at once, which constitutes an appropriate upper bound on the average number of relevant features per class $n_{wc} = \frac{n_w}{n_c}$. In our work we focus on $n_{wc} \leq 5$.

The pipeline of our approach is presented in Figure 2 and utilizes *glm-saga* for sparsification and feature selection. We first train a deep neural network with our proposed feature diversity loss $\mathcal{L}_{\text{div}}$ until convergence. Then the features $\boldsymbol{F}^{\text{train}} \in \mathbb{R}^{n_T\times n_f}$ for all n_T images in the training set are computed, which are the average pooled feature maps $\boldsymbol{M}$. Afterwards, the features are selected as described in Section 3.2.2 and *glm-saga*, presented in Section 2.2.1, is used to calculate the regularization path. Finally, the solution with the desired sparsity is selected from the regularization path and the remaining layers get finetuned with the final layer set to the sparse model, s. t. the features adapt to it.

3.2.1 Feature Diversity Loss

The goal of the proposed feature diversity loss $\mathcal{L}_{\text{div}}$ is that every feature captures a different independent concept. This is achieved by enforcing differently localized features in their feature maps. The proposed loss is motivated by the *Mutual-Channel Loss* (MCL) (Chang et al., 2020) and the *Feature Redundancy loss* (FRL) (Zheng et al., 2020). In contrast to FRL, we use Cross-Channel-Max-Pooling (CCMP) (Goodfellow et al., 2013) over all weighted feature maps to optimize all features jointly and reduce the need for the hyperparameter K. MCL also uses CCMP but instead of grouping the channels into class-specific filters, we apply the diversity component to all feature maps $\boldsymbol{M}$, to aim for shared interpretable features. For notation, $w_{\hat{c}l}$ describes the entry in $\boldsymbol{W}$ that is assigned to the specific feature $l \in \{0, 1, \ldots, n_f - 1\}$ for the predicted class $\hat{c} = \arg\max(\boldsymbol{y})$ and $m_{ij}^l = \boldsymbol{M}_{l,i,j}$.

$$\hat{s}_{ij}^l = \frac{\exp(m_{ij}^l)}{\sum_{i'=1}^{h_M}\sum_{j'=1}^{w_M}\exp(m_{i'j'}^l)} \frac{f_l}{\max \boldsymbol{f}} \frac{|w_{\hat{c}l}|}{\|\boldsymbol{w}_{\hat{c}}\|_2} \tag{3}$$

$$\mathcal{L}_{\text{div}} = -\sum_{i=1}^{h_M}\sum_{j=1}^{w_M}\max(\hat{s}_{ij}^1, \hat{s}_{ij}^2, \ldots, \hat{s}_{ij}^{n_f}) \tag{4}$$

Dataset	CUB-2011	Stanford Cars	FGVC-Aircraft	NABirds	ImageNet-1K
#Classes n_c	200	196	100	555	1 000
Training	5 994	8 144	6 667	23 929	1 281 167
Testing	5 774	8 041	3 333	24 633	50 000

Table 1: Overview of the number of classes, training and testing examples for the used datasets

Method	Additional Supervision required	Features trained end-to-end	n_f^* ↓	n_{wc} ↓	ImageNet-1K ↑	CUB-2011 ↑
CBM (Koh et al., 2020) - joint	✓	✓	112	112	-	80.1 (76.8*)
CBM (Koh et al., 2020) - independent	✓	✗	112	112	-	76.0
CBM-AUC (Sawada and Nakamura, 2022)	✓	✓	256	256	-	**82.3**
glm-saga (Wong et al., 2021)	✗	✓	n_f	$\leq$ **5**	58.0*	76.1 (78.0*)
SLDD-Model (**Ours**) with $n_f^* = n_f$	✗	✓	n_f	**5**	**76.7***	80.3 (**86.5***)
SLDD-Model (**Ours**)	✗	✓	**50**	**5**	**72.8***	78.3 (**84.0***)

Table 2: Comparison with competitors on accuracy in percent. For ease of comparison, we evaluated CUB-2011 on Inception-v3 ($n_f = 1024$) and ImageNet-1K with Resnet50 ($n_f = 2048$) (*denotes Resnet50 accuracy). The dense Resnet50 achieves $80.9\,\%$ on ImageNet-1K. For *glm-saga*, we selected the solution with maximum $n_{wc} \leq 5$. Arrows indicate generally preferable directions. For *CBM - joint*, Resnet50 results were created as described in Appendix B.1.1

Equation 3 uses the softmax to transform the feature maps $\boldsymbol{M}$ by normalizing their entries m_{ij}^l over the spatial dimensions and then scales the maps so that they focus on visible and important features by maintaining the relative mean of $\boldsymbol{M}$ while weighting them according to the predicted class, s. t. different to MCL absent features do not have to be localized in small background patches. Equation 4 decreases the loss if the different weighted feature maps $\hat{S}^l$ attend to different locations. The final training loss is then $\mathcal{L}_{\text{final}} = \mathcal{L}_{CE} + \beta \mathcal{L}_{\text{div}}$ with the weighting factor $\beta \in \mathbb{R}_+$.

3.2.2 Feature Selection

For selecting the set of features N_{f^*} from the initial features N_f s. t. $|N_{f^*}| = n_f^*$, we run an adapted version of *glm-saga*, introduced in Section 2.2.1, until one solution $(\boldsymbol{W}_j^{\text{sparse}}, \boldsymbol{b}_j)$ of the regularization path uses a feature not already in N_{f^*}, which we then add to the set of selected features N_{f^*} and restart the adapted *glm-saga*. As adaptation, we extended the proximal operator of the group version of *glm-saga*, which operates on $\boldsymbol{w}_l = \boldsymbol{W}_{:,l}$, which are the entries in $\boldsymbol{W}$ that correspond to an entire feature l. Since $\|\boldsymbol{w}_l\|_2$ indicates the importance of l, we additionally only keep entries for features that have the maximum norm or are in N_{f^*}, s. t. exactly one feature is added per iteration. The resulting proximal operator with $\lambda_1 = \gamma\lambda\alpha$ and $\lambda_2 = \gamma\lambda(1-\alpha)$ is:

$$\text{Prox}_{\lambda_1,\lambda_2}(\boldsymbol{w}_i) = \begin{cases} \frac{\boldsymbol{w}_i(\|\boldsymbol{w}_i\|_2 - \lambda_1)}{(1+\lambda_2)\|\boldsymbol{w}_i\|_2} & \text{if } \|\boldsymbol{w}_i\|_2 > \lambda_1 \underline{\wedge \|\boldsymbol{w}_i\|_2 = \max_{j' \in N_f \setminus N_{f^*}} \|\boldsymbol{w}_{j'}\|_2 \vee i \in N_{f^*}} \\ \boldsymbol{0} & \text{otherwise} \end{cases} \tag{5}$$

The extensions are underlined and γ is the learning rate of *glm-saga*.

4 Experiments

This section contains our experimental results. We validate our method using Resnet50 (He et al., 2016), DenseNet121 (Huang et al., 2017) and Inception-v3 (Szegedy et al., 2016) on four common benchmark datasets in the domain of fine-grained image classification. Additionally, we show the applicability of a *SLDD-Model* for large scale datasets like ImageNet-1K (Russakovsky et al., 2015). An overview of CUB-2011 (Wah et al., 2011), Stanford Cars (Krause et al., 2013), FGVC-Aircraft (Maji et al., 2013), NABirds (Van Horn et al., 2015) and ImageNet-1K is given in Table 1. Additionally, CUB-2011 contains labels for the images such as attributes (*e.g.* "red wing") as well as for the classes, which makes it easier to measure the alignment with understandable concepts. After the competitive accuracy and the impact of $\mathcal{L}_{\text{div}}$ is shown, the interpretability of the *SLDD-Model* is discussed and these attributes are used to show the alignment of the learned features. The implementation details can be found in Appendix B.1. Finally, the tradeoff between interpretability and accuracy is visualized.

	CUB-2011					FGVC-Aircraft					NABirds					Stanford Cars				
	$n_f^* = 2048$			$n_f^* = 50$		$n_f^* = 2048$			$n_f^* = 50$		$n_f^* = 2048$			$n_f^* = 50$		$n_f^* = 2048$			$n_f^* = 50$	
$\mathcal{L}_{\text{div}}$	Dense	Sparse	Finet.	Sparse	Finet.	Dense	Sparse	Finet.	Sparse	Finet.	Dense	Sparse	Finet.	Sparse	Finet.	Dense	Sparse	Finet.	Sparse	Finet.
✗	86.6	81.8	85.3	79.5	83.4	90.0	88.4	89.4	87.3	88.1	84.2	79.5	83.3	77.3	80.7	93.2	90.9	92.6	89.3	91.1
✓	86.6	**84.0**	**86.5**	**81.7**	**84.0**	**91.4**	**90.7**	**91.1**	**89.8**	**90.1**	**84.4**	**81.0**	**84.0**	**79.8**	**81.7**	**93.6**	**92.1**	**93.3**	**91.1**	**92.0**
MCL Chang et al. (2020)	86.1	81.9	85.1	79.4	82.8	90.1	88.4	89.0	87.2	88.1	-	-	-	-	-	93.1	91.0	92.5	89.0	90.7
FRL Zheng et al. (2020)	86.4	81.5	85.3	78.9	82.6	90.0	88.5	89.4	87.5	88.2	-	-	-	-	-	93.3	90.8	92.6	89.4	90.9

Table 3: Impact of the loss function on accuracy in percent for Resnet50. Best results are in bold.

	CUB-2011					FGVC-Aircraft					NABirds					Stanford Cars				
	$n_f^* = n_f$			$n_f^* = 50$		$n_f^* = n_f$			$n_f^* = 50$		$n_f^* = n_f$			$n_f^* = 50$		$n_f^* = n_f$			$n_f^* = 50$	
Backbone	Dense	Sparse	Finet.	Sparse	Finet.	Dense	Sparse	Finet.	Sparse	Finet.	Dense	Sparse	Finet.	Sparse	Finet.	Dense	Sparse	Finet.	Sparse	Finet.
DenseNet121	86.3	76.2	82.9	75.7	83.1	**91.5**	88.2	89.8	88.1	90.0	84.1	72.8	64.6	71.0	80.5	93.3	87.3	91.7	85.8	91.4
Inception-v3	82.3	78.0	80.3	74.0	78.3	88.9	87.5	88.1	85.9	87.4	79.0	75.8	77.3	73.1	76.5	91.5	88.9	90.3	86.3	89.4
Resnet50	**86.6**	**84.0**	**86.5**	**81.7**	**84.0**	91.4	**90.7**	**91.1**	**89.8**	**90.1**	**84.4**	**81.0**	**84.0**	**79.8**	**81.7**	**93.6**	**92.1**	**93.3**	**91.1**	**92.0**

Table 4: Accuracy in percent dependent on backbone. Best results are in bold.

4.1 Diversity Metric

To assess the impact of $\mathcal{L}_{\text{div}}$, we developed a measurement for the local diversity of the feature maps $\boldsymbol{M}$ that led to the decision, inspired by the diversity component of MCL (Chang et al., 2020), which entails a different way of computing the features. For that, we consider the k feature maps $\boldsymbol{M}_k$ that are weighted the highest for the predicted class $\hat{c}$ in $\boldsymbol{W}$. To only compare the localization, softmax is applied to the $\boldsymbol{M}_k$, yielding $\boldsymbol{S}_k$. With these distributions $\boldsymbol{S}_k$, we compute the diversity as

$$\text{diversity@k} = \frac{\sum_{i=1}^{h_M} \sum_{j=1}^{w_M} \max(s_{ij}^1, s_{ij}^2, \ldots, s_{ij}^k)}{k} \tag{6}$$

with diversity@k $\in [\frac{1}{k}, 1]$ to measure how different and pronounced the $\boldsymbol{M}_k$ are localized. Since we focus on $n_{wc} \leq 5$, we set $k = 5$. We report the mean diversity@5 for all classes that use at least five features. Note that the proposed $\mathcal{L}_{\text{div}}$ is a weighted version of diversity@n_f.

4.2 Results

We report the accuracy on the test set for the dense model after training the pretrained model on the training data with $n_{wc} = n_f$, for the sparse model with $n_{wc} \leq 5$, and for the result of our whole pipeline, the model with finetuned features, obtained by training the sparse model on the training data, and still $n_{wc} \leq 5$. Every shown metric is the average over five (four for ImageNet-1K) randomly seeded runs. The standard deviations are included in the appendix.

Table 3 shows the competitive performance of our *SLDD-Model* to the dense Resnet50. It is evident that an extreme sparsity of $s = \frac{5}{2048}$ can be obtained in the final layer with just 0.1 to 0.4 percent points less accuracy. Additionally decreasing the number of features by $97.6\,\%$, resulting in just 50 instead of the previous 2048 features, only reduces the accuracy compared to the dense model by 1.3 to 2.7 percent points. Finally, our proposed $\mathcal{L}_{\text{div}}$ improves the accuracy for all sparse models. Table 4 shows the general applicability of our method with different backbones. However, we observed some instability and no increased accuracy when finetuning the DenseNet121 with $n_f^* = 2048$, showing a positive effect of sharing features. Table 2 compares our approach to competitors: Without requiring additional supervision, we achieve a competitive performance compared to *CBM* (Koh et al., 2020)-based methods, while achieving a lower dimensionality and higher sparsity. Additionally, we improve the accuracy of *glm-saga* with heavily reduced n_f^*. For ImageNet-1K, we skipped the dense training and directly used the pretrained model. The good scalability of our proposed method to this large dataset with a higher number of classes is displayed in Table 5. Table 6 shows the diversity@5: With $\mathcal{L}_{\text{div}}$ it is very close to the maximum value of $100\,\%$ in the dense case and still heavily increased in the sparse cases. This showcases that $\mathcal{L}_{\text{div}}$ is suitable to ensure a diverse localization and improved interpretability of the used feature maps , which is visualized in Figures 9 to 17. Finally, the total number of features that is used by the unrestricted ($n_f^* = n_f$) models in Table 3 is reduced from 912 to 719 for the models with $\mathcal{L}_{\text{div}}$, but still shows a high number of class-specific features. That $\mathcal{L}_{\text{div}}$ leads to more shared features supports our motivation of enforcing different features to capture different concepts.

Dense ($n_f^* = 2048$)	Sparse ($n_f^* = 2048$)	Finet. ($n_f^* = 2048$)	Sparse ($n_f^* = 50$)	Finet. ($n_f^* = 50$)
80.9	62.2	76.7	44.8	72.8

Table 5: Accuracy in percent for Resnet50 on ImageNet-1K using the pretrained dense model.

	CUB-2011					FGVC-Aircraft					Stanford Cars				
	$n_f^* = 2048$			$n_f^* = 50$		$n_f^* = 2048$			$n_f^* = 50$		$n_f^* = 2048$			$n_f^* = 50$	
$\mathcal{L}_{\text{div}}$	Dense	Sparse	Finet.	Sparse	Finet.	Dense	Sparse	Finet.	Sparse	Finet.	Dense	Sparse	Finet.	Sparse	Finet.
✗	50.2	46.0	43.4	48.0	46.5	46.5	43.8	40.9	45.9	44.0	45.0	41.7	39.1	43.6	43.7
✓	**98.9**	**69.9**	**71.9**	**65.2**	**72.6**	**98.8**	**85.7**	**86.6**	**69.3**	**73.9**	**99.2**	**72.4**	**74.6**	**63.7**	**74.8**
MCL Chang et al. (2020)	52.5	51.4	48.9	56.7	52.3	50.1	50.6	48.3	51.7	50.1	49.0	49.0	46.2	51.8	49.5
FRL Zheng et al. (2020)	51.1	47.1	44.1	49.0	46.3	48.2	44.6	41.2	44.9	43.1	46.2	43.0	40.0	43.0	41.7

Table 6: Impact of the loss function on diversity@5 in percent for Resnet50. Best results are in bold.

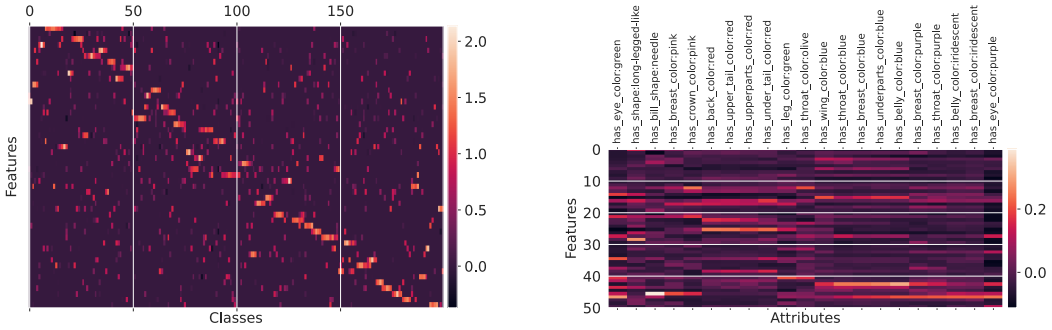

(a) Exemplary $\boldsymbol{W}^{\text{sparse}}$. The alignment of the features with attributes in CUB-2011 is displayed in Figure 3b.

(b) Relationship between chosen features and attributes ($C > 20\%$) of CUB-2011 for the exemplary model. Higher values indicate that the feature describes the attribute.

Figure 3: Visualization of the sparse matrix and the feature alignment.

4.2.1 Comparison with Other Loss Functions

We compare our diversity loss $\mathcal{L}_{\text{div}}$ with the MCL (Chang et al., 2020) and the FRL (Zheng et al., 2020). The used hyperparameters for the loss functions are reported in Appendix B.1.1 and we focussed on three datasets to save computational resources. Table 3 shows that our $\mathcal{L}_{\text{div}}$ reaches the highest accuracy across all datasets. Notably, the accuracy reported in (Chang et al., 2020) for the MC-Loss is achieved by a two-layer MLP plus additional techniques, whereas we only use one layer to ensure linearly separable representations for our *SLDD-Model*. Although it is expected that applying $\mathcal{L}_{\text{div}}$ has a positive effect on diversity@5 due to the similar formulation, we could observe a remarkable uplift in diversity@5 (Table 6) compared to MCL and FRL, which also optimize for differently localized features.

4.3 Interpretability

In this section, we discuss the interpretability of the proposed *SLDD-Model* using example models. The interpretability of the proposed *SLDD-Model* is based upon using very few (n_{wc}) features from a small pool of n_f^* to make a decision. A low n_f^* allows the analysis of the remaining features to try to align them with a human understandable concept, which is discussed in Section 4.3.1. Since the sparse linear layer is easily interpretable, the complete model with sufficiently well understood features is both **locally** and **globally** interpretable.

For **global interpretability**, the final layer of the *SLDD-Model* can be fully visualized and analyzed. Figure 3a shows $\boldsymbol{W}^{\text{sparse}}$. This allows the practitioner to verify the global behavior of the model. For example, the attribute aligned with "has-bill-shape:needle" in the presented model in Section 4.3.1 has a non-zero weight for all four classes that have the attribute in more than 30 % of examples. The visualization of the classes positively related to a specific attribute and features related to a class like Figures 9 to 17 helps to trust the model. Additionally, $\boldsymbol{W}^{\text{sparse}}$ allows for further feature understanding, since it is possible to analyze the similarities between classes that share a feature. If the feature is aligned well, this leads to knowledge discovery.

The **local interpretability** describes the explanation of a single decision made by the model. Decisions with sparsely connected features are inherently locally interpretable, if the features can be interpreted and localized, as shown in Figure 1. The practitioner can understand where and what was found in the image, and due to the full global interpretability also understand the behavior around the current example.

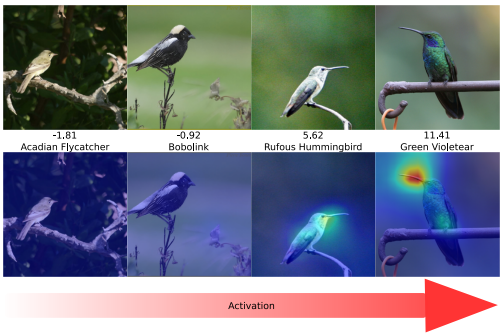

(a) Feature 45 with $C = 0.39$ for the attribute "has-bill-shape:needle": Higher activations are localized around the bill, and a needle-like bill is visible.

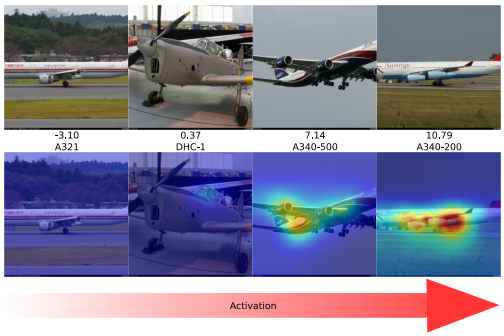

(b) Manually aligned feature of a model trained on FGVC-Aircraft without additional labels: The feature is manually aligned with four engine aircraft as shown in Appendix E.

Figure 4: Example images and localization $\boldsymbol{L}$, scaled to indicate feature activation, in ascending order for two models. The text between the rows describes the activation value for the image, which drops below 0 due to the normalization of *glm-saga*, and the class name.

4.3.1 Feature Alignment

In this section, we demonstrate how the features of the proposed *SLDD-Model* can be aligned with interpretable concepts.We describe how one can use additional labels or expert knowledge to interpret the features and demonstrate that several learned sparse features are directly connected to attributes relevant to humans. Thus, our model learns such abstract concepts directly from the data. Overall, due to the very limited number of used features n_f^*, the features can and should be thoroughly analyzed and interpreted to facilitate interpretability. For feature localization, we follow a masking approach similar to Fong and Vedaldi (2017), which is described in Appendix D.

Alignment with Additional Data We use the attributes A contained in CUB-2011 to align the learned features with these labels after the finetuning. For each attribute $a \in A$ and feature j we compute a score C_{aj} that corresponds to a relative increase of the feature when the attribute is present:

$$\delta_{aj} = \frac{1}{|\rho_{a+}|} \sum_{i \in \rho_{a+}} \boldsymbol{F}^{\text{train}}_{i,j} - \frac{1}{|\rho_{a-}|} \sum_{i \in \rho_{a-}} \boldsymbol{F}^{\text{train}}_{i,j} \qquad C_{aj} = \frac{\delta_{aj}}{\max(\boldsymbol{F}^{\text{train}}_{:,j}) - \min(\boldsymbol{F}^{\text{train}}_{:,j})} \tag{7}$$

The set of indices whose images contain the attribute is denoted by ρ_{a+}. We considered an attribute to be present if the human annotated it with "probably" or "definitely". Annotations with "guessing" were neither included in the positive (ρ_{a+}) nor negative (ρ_{a-}) examples. For one exemplary model a part of the matrix of C values is displayed in Figure 3b. It is clear, that some features correspond to colors, some to specific shapes like "bill-shape:needle" and other features do not correlate with specific attributes. Figure 4a visually validates the connection that was implied in Figure 3b.

Manual Alignment To ensure that the entirety of a feature is understood, or in absence of additional data, the features have to be manually aligned for increased interpretability. This is enabled by the low number of features and sparsity. Some useful aspects for understanding a feature are the localization, extreme examples, feature visualization (Olah et al., 2017) or which classes use that feature. One such alignment for a model trained on FGVC-Aircraft is displayed in Appendix E and Figure 4b. Aligning learned features with human understandable concepts is still challenging as a single feature can refer to multiple aspects and human understandable concepts do not need to be axis aligned (Szegedy et al., 2013). However, the low dimensionality of the remaining features allows for a sophisticated analysis of every feature in practice, which could even discover spurious correlations as features as done by the *glm-saga* publication.

4.4 Interpretability Tradeoff

In this section, we analyze the impact of changing n_f^* and n_{wc} on the finetuning accuracy of the model trained with $\mathcal{L}_{\text{div}}$, shown in Figure 5. Figure 5a visualizes the impact of n_f^*: With decreasing n_f^* the accuracy drops slowly until a dataset-specific threshold is reached, at which a steep decline

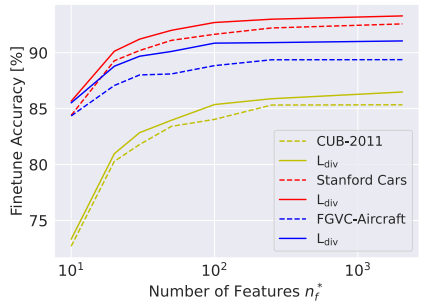

(a) Impact of changing n_f^* with $n_{wc} = 5$

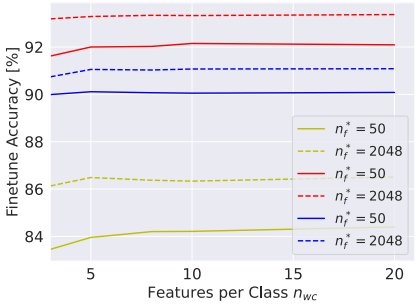

(b) Impact of changing n_{wc} with $n_f^* = 50$ or 2048

Figure 5: Relationship between Finetune Accuracy and aspects related to interpretability for Resnet50.

starts. Additionally, the proposed $\mathcal{L}_{\text{div}}$ works regardless of n_f^*. Figure 5b shows the finetuning accuracy in relation to n_{wc}: The accuracy is rather insensitive to n_{wc}, only decreasing when $n_{wc} < 5$, which is the case for both dimensions and showcases that five features suffice for a competitive model even if the features are shared among classes. Figure 5 demonstrates the tradeoff that our *SLDD-Model* offers: Both n_{wc} and n_f^* can be drastically reduced with either a negligible or small impact on accuracy to adapt to the amount of interpretability needed.

5 Limitations and Future Work

As shown in Figure 5, the *SLDD-Model* cannot get arbitrarily low-dimensional or sparse with competitive accuracy via our proposed method. The optimal sparsity and dimensionality for a given problem are hard to predict and might require some experiments to determine the minimum values for competitive accuracy. Aligning all used features with human concepts is still difficult, albeit more feasible than without a *SLDD-Model*. Future work could use a more interpretable feature extractor like *B-cos Networks* (Böhle et al., 2022) to alleviate that problem. The method could be improved via the feature selection or improvements for small datasets (Reinders et al., 2022). It seems promising to apply a *SLDD-Model* to other safety-critical domains, such as medical, where an expert can be utilized to align the features and follow the decision, as it can help bring the required interpretability and trustworthiness to the domain. Embodied autonomous agents can also benefit from it, as the entire decision process can be thoroughly analyzed. In this domain, our approach could be extended to anomaly detection (Rudolph et al., 2022) in addition to classification. While more interpretable models could be used to more deliberately bring harm, they can disclose existing problems with machine learning models and open up the opportunity to build fair and trustworthy models. Finally, sparsity and dimensionality could be part of metrics used to quantify the trustworthiness of a model.

6 Conclusion

In this work, we proposed the more interpretable sparse low-dimensional decision model (*SLDD-Model*) to allow a human to follow and understand the decision of a Deep Neural Network for image classification. Our proposed pipeline constructs a *SLDD-Model* with drastically increased global and local interpretability while still showing competitive accuracy. As demonstrated, a practitioner can manually configure the pipeline to set the tradeoff between accuracy and interpretability. Our novel loss increases the feature diversity and we showed that identifying a class with varied features can improve the accuracy. Finally, our *SLDD-Model* offers measurable aspects of interpretability, which allows future work to not just compare itself on accuracy but also on interpretability.

Acknowledgements. This work was supported by the Federal Ministry of Education and Research (BMBF), Germany under the project LeibnizKILabor (grant no. 01DD20003), the Center for Digital Innovations (ZDIN) and the Deutsche Forschungsgemeinschaft (DFG) under Germany's Excellence Strategy within the Cluster of Excellence PhoenixD (EXC 2122).

References

Julius Adebayo, Justin Gilmer, Michael Muelly, Ian Goodfellow, Moritz Hardt, and Been Kim. Sanity checks for saliency maps. *Advances in neural information processing systems*, 31, 2018.

David Bau, Bolei Zhou, Aditya Khosla, Aude Oliva, and Antonio Torralba. Network dissection: Quantifying interpretability of deep visual representations. In *Proceedings of the IEEE conference on computer vision and pattern recognition*, pages 6541–6549, 2017.

Adrien Bibal, Michael Lognoul, Alexandre Streel, and Benoît Frénay. Legal requirements on explainability in machine learning. *Artificial Intelligence and Law*, 29, 06 2021.

Moritz Böhle, Mario Fritz, and Bernt Schiele. B-cos networks: Alignment is all we need for interpretability. In *Proceedings of the IEEE/CVF Conference on Computer Vision and Pattern Recognition*, pages 10329–10338, 2022.

Dongliang Chang, Yifeng Ding, Jiyang Xie, Ayan Kumar Bhunia, Xiaoxu Li, Zhanyu Ma, Ming Wu, Jun Guo, and Yi-Zhe Song. The Devil is in the Channels: Mutual-Channel Loss for Fine-Grained Image Classification. *IEEE Transactions on Image Processing*, 29:4683–4695, 2020.

Dongliang Chang, Kaiyue Pang, Yixiao Zheng, Zhanyu Ma, Yi-Zhe Song, and Jun Guo. Your "Flamingo" is My "Bird": Fine-Grained, or Not. *2021 IEEE/CVF Conference on Computer Vision and Pattern Recognition (CVPR)*, 00:11471–11480, 2021.

Chaofan Chen, Oscar Li, Daniel Tao, Alina Barnett, Cynthia Rudin, and Jonathan K Su. This looks like that: deep learning for interpretable image recognition. *Advances in neural information processing systems*, 32, 2019.

Tianshui Chen, Wenxi Wu, Yuefang Gao, Le Dong, Xiaonan Luo, and Liang Lin. Fine-grained representation learning and recognition by exploiting hierarchical semantic embedding. In *Proceedings of the 26th ACM international conference on Multimedia*, pages 2023–2031, 2018.

Po-Yung Chou, Cheng-Hung Lin, and Wen-Chung Kao. A Novel Plug-in Module for Fine-Grained Visual Classification. *arXiv*, 2022.

Alexander Dockhorn and Rudolf Kruse. Fuzzy modeling in game ai. *Journal of Pure and Applied Mathematics*, 12(1):54–68, 2021.

Logan Engstrom, Andrew Ilyas, Hadi Salman, Shibani Santurkar, and Dimitris Tsipras. Robustness (python library), 2019.

Ruth C Fong and Andrea Vedaldi. Interpretable explanations of black boxes by meaningful perturbation. In *Proceedings of the IEEE international conference on computer vision*, pages 3429–3437, 2017.

Sorelle A Friedler, Chitradeep Dutta Roy, Carlos Scheidegger, and Dylan Slack. Assessing the local interpretability of machine learning models. 2019.

Jerome Friedman, Trevor Hastie, and Rob Tibshirani. Regularization paths for generalized linear models via coordinate descent. *Journal of statistical software*, 33(1):1, 2010.

Trevor Gale, Erich Elsen, and Sara Hooker. The state of sparsity in deep neural networks. *arXiv preprint arXiv:1902.09574*, 2019.

Nidham Gazagnadou, Robert Gower, and Joseph Salmon. Optimal mini-batch and step sizes for saga. In *International conference on machine learning*, pages 2142–2150. PMLR, 2019.

Ian Goodfellow, David Warde-Farley, Mehdi Mirza, Aaron Courville, and Yoshua Bengio. Maxout networks. In *International conference on machine learning*, pages 1319–1327. PMLR, 2013.

Kaiming He, Xiangyu Zhang, Shaoqing Ren, and Jian Sun. Deep residual learning for image recognition. In *Proceedings of the IEEE conference on computer vision and pattern recognition*, pages 770–778, 2016.

Adrian Hoffmann, Claudio Fanconi, Rahul Rade, and Jonas Kohler. This looks like that... does it? shortcomings of latent space prototype interpretability in deep networks. *arXiv preprint arXiv:2105.02968*, 2021.

Gao Huang, Zhuang Liu, Laurens Van Der Maaten, and Kilian Q Weinberger. Densely connected convolutional networks. In *Proceedings of the IEEE conference on computer vision and pattern recognition*, pages 4700–4708, 2017.

Sheikh Rabiul Islam, William Eberle, and Sheikh K Ghafoor. Towards quantification of explainability in explainable artificial intelligence methods. In *The thirty-third international flairs conference*, 2020.

Saachi Jain, Hadi Salman, Eric Wong, Pengchuan Zhang, Vibhav Vineet, Sai Vemprala, and Aleksander Madry. Missingness bias in model debugging. In *International Conference on Learning Representations*, 2022.

Been Kim, Martin Wattenberg, Justin Gilmer, Carrie Cai, James Wexler, Fernanda Viegas, et al. Interpretability beyond feature attribution: Quantitative testing with concept activation vectors (tcav). In *International conference on machine learning*, pages 2668–2677. PMLR, 2018.

Sunnie SY Kim, Nicole Meister, Vikram V Ramaswamy, Ruth Fong, and Olga Russakovsky. Hive: evaluating the human interpretability of visual explanations. *arXiv preprint arXiv:2112.03184*, 2021.

Pieter-Jan Kindermans, Sara Hooker, Julius Adebayo, Maximilian Alber, Kristof T Schütt, Sven Dähne, Dumitru Erhan, and Been Kim. The (un) reliability of saliency methods. In *Explainable AI: Interpreting, Explaining and Visualizing Deep Learning*, pages 267–280. Springer, 2019.

Pang Wei Koh, Thao Nguyen, Yew Siang Tang, Stephen Mussmann, Emma Pierson, Been Kim, and Percy Liang. Concept bottleneck models. In *International Conference on Machine Learning*, pages 5338–5348. PMLR, 2020.

Jonathan Krause, Michael Stark, Jia Deng, and Li Fei-Fei. 3d object representations for fine-grained categorization. In *4th International IEEE Workshop on 3D Representation and Recognition (3dRR-13)*, Sydney, Australia, 2013.

Haoyu Liang, Zhihao Ouyang, Yuyuan Zeng, Hang Su, Zihao He, Shu-Tao Xia, Jun Zhu, and Bo Zhang. Training interpretable convolutional neural networks by differentiating class-specific filters. In *European Conference on Computer Vision*, pages 622–638. Springer, 2020.

Tsung-Yu Lin, Aruni RoyChowdhury, and Subhransu Maji. Bilinear cnn models for fine-grained visual recognition. In *Proceedings of the IEEE international conference on computer vision*, pages 1449–1457, 2015.

S. Maji, J. Kannala, E. Rahtu, M. Blaschko, and A. Vedaldi. Fine-grained visual classification of aircraft. Technical report, 2013.

Andrei Margeloiu, Matthew Ashman, Umang Bhatt, Yanzhi Chen, Mateja Jamnik, and Adrian Weller. Do concept bottleneck models learn as intended? *arXiv preprint arXiv:2105.04289*, 2021.

Thomas McGrath, Andrei Kapishnikov, Nenad Tomašev, Adam Pearce, Demis Hassabis, Been Kim, Ulrich Paquet, and Vladimir Kramnik. Acquisition of Chess Knowledge in AlphaZero. *arXiv*, 2021.

George A Miller. The magical number seven, plus or minus two: Some limits on our capacity for processing information. *Psychological review*, 63(2):81, 1956.

Christoph Molnar. *Interpretable machine learning*. Lulu. com, 2020.

Meike Nauta, Ron van Bree, and Christin Seifert. Neural prototype trees for interpretable fine-grained image recognition. In *Proceedings of the IEEE/CVF Conference on Computer Vision and Pattern Recognition*, pages 14933–14943, 2021.

Chris Olah, Alexander Mordvintsev, and Ludwig Schubert. Feature visualization. *Distill*, 2(11):e7, 2017.

Adam Paszke, Sam Gross, Francisco Massa, Adam Lerer, James Bradbury, Gregory Chanan, Trevor Killeen, Zeming Lin, Natalia Gimelshein, Luca Antiga, Alban Desmaison, Andreas Kopf, Edward Yang, Zachary DeVito, Martin Raison, Alykhan Tejani, Sasank Chilamkurthy, Benoit Steiner, Lu Fang, Junjie Bai, and Soumith Chintala. Pytorch: An imperative style, high-performance deep learning library. In H. Wallach, H. Larochelle, A. Beygelzimer, F. d'Alché-Buc, E. Fox, and R. Garnett, editors, *Advances in Neural Information Processing Systems 32*, pages 8024–8035. Curran Associates, Inc., 2019.

Vikram V Ramaswamy, Sunnie S Y Kim, Nicole Meister, Ruth Fong, and Olga Russakovsky. ELUDE: Generating interpretable explanations via a decomposition into labelled and unlabelled features. *arXiv*, 2022. Decomposition in unlabelled / labelled features. Sparse explanation, not prediction as it uses ground truth attribute labels for explanation. Does not have to be faithful with actually done prediction.

Christoph Reinders, Frederik Schubert, and Bodo Rosenhahn. Chimeramix: Image classification on small datasets via masked feature mixing. In Lud De Raedt, editor, *Proceedings of the Thirty-First International Joint Conference on Artificial Intelligence, IJCAI-22*, pages 1298–1305. International Joint Conferences on Artificial Intelligence Organization, 7 2022. Main Track.

Pratyush Rokade and BKSP Kumar Raju Alluri. Towards quantification of explainability algorithms. In *2021 The 5th International Conference on Advances in Artificial Intelligence (ICAAI)*, pages 31–37, 2021.

Marco Rudolph, Tom Wehrbein, Bodo Rosenhahn, and Bastian Wandt. Fully convolutional cross-scale-flows for image-based defect detection. In *Proceedings of the IEEE/CVF Winter Conference on Applications of Computer Vision (WACV)*, pages 1088–1097, January 2022.

Stefan Rüping et al. Learning interpretable models. 2006.

Olga Russakovsky, Jia Deng, Hao Su, Jonathan Krause, Sanjeev Satheesh, Sean Ma, Zhiheng Huang, Andrej Karpathy, Aditya Khosla, Michael Bernstein, Alexander C. Berg, and Li Fei-Fei. ImageNet Large Scale Visual Recognition Challenge. *International Journal of Computer Vision (IJCV)*, 115(3):211–252, 2015.

Dawid Rymarczyk, Łukasz Struski, Michał Górszczak, Koryna Lewandowska, Jacek Tabor, and Bartosz Zieliński. Interpretable image classification with differentiable prototypes assignment. In *European Conference on Computer Vision*, pages 351–368. Springer, 2022.

Dawid Rymarczyk, Łukasz Struski, Jacek Tabor, and Bartosz Zieliński. Protopshare: Prototypical parts sharing for similarity discovery in interpretable image classification. In *Proceedings of the 27th ACM SIGKDD Conference on Knowledge Discovery & Data Mining*, pages 1420–1430, 2021.

Yoshihide Sawada and Keigo Nakamura. Concept Bottleneck Model With Additional Unsupervised Concepts. *IEEE Access*, 10:41758–41765, 2022.

Ramprasaath R Selvaraju, Michael Cogswell, Abhishek Das, Ramakrishna Vedantam, Devi Parikh, and Dhruv Batra. Grad-cam: Visual explanations from deep networks via gradient-based localization. In *Proceedings of the IEEE international conference on computer vision*, pages 618–626, 2017.

Christian Szegedy, Vincent Vanhoucke, Sergey Ioffe, Jon Shlens, and Zbigniew Wojna. Rethinking the inception architecture for computer vision. In *Proceedings of the IEEE conference on computer vision and pattern recognition*, pages 2818–2826, 2016.

Christian Szegedy, Wojciech Zaremba, Ilya Sutskever, Joan Bruna, Dumitru Erhan, Ian Goodfellow, and Rob Fergus. Intriguing properties of neural networks. *arXiv preprint arXiv:1312.6199*, 2013.

Hong Tao, Chenping Hou, Feiping Nie, Yuanyuan Jiao, and Dongyun Yi. Effective discriminative feature selection with nontrivial solution. *IEEE transactions on neural networks and learning systems*, 27(4):796–808, 2015.

Kale-ab Tessera, Sara Hooker, and Benjamin Rosman. Keep the gradients flowing: Using gradient flow to study sparse network optimization. *arXiv preprint arXiv:2102.01670*, 2021.

Grant Van Horn, Steve Branson, Ryan Farrell, Scott Haber, Jessie Barry, Panos Ipeirotis, Pietro Perona, and Serge Belongie. Building a bird recognition app and large scale dataset with citizen scientists: The fine print in fine-grained dataset collection. In *2015 IEEE Conference on Computer Vision and Pattern Recognition (CVPR)*, pages 595–604, 2015.

Catherine Wah, Steve Branson, Peter Welinder, Pietro Perona, and Serge Belongie. The caltech-ucsd birds-200-2011 dataset. 2011.

Eric Wong, Shibani Santurkar, and Aleksander Madry. Leveraging sparse linear layers for debuggable deep networks. In *International Conference on Machine Learning*, pages 11205–11216. PMLR, 2021.

Hongyu Yang, Cynthia Rudin, and Margo Seltzer. Scalable bayesian rule lists. In *International conference on machine learning*, pages 3921–3930. PMLR, 2017.

Mert Yuksekgonul, Maggie Wang, and James Zou. Post-hoc concept bottleneck models. In *ICLR 2022 Workshop on PAIR^2Struct: Privacy, Accountability, Interpretability, Robustness, Reasoning on Structured Data*, 2022.

Matthew D Zeiler and Rob Fergus. Visualizing and understanding convolutional networks. In *European conference on computer vision*, pages 818–833. Springer, 2014.

Runkai Zheng, Zhijia Yu, Yinqi Zhang, Chris Ding, Hei Victor Cheng, and Li Liu. Learning Class Unique Features in Fine-Grained Visual Classification. *arXiv*, 2020.

Hui Zou and Trevor Hastie. Regularization and variable selection via the elastic net. *Journal of the Royal Statistical Society: Series B (Statistical Methodology)*, 67(2):301–320, 2005.

	CUB-2011					FGVC-Aircraft					NABirds					Stanford Cars				
	$n_f^* = 2048$			$n_f^* = 50$		$n_f^* = 2048$			$n_f^* = 50$		$n_f^* = 2048$			$n_f^* = 50$		$n_f^* = 2048$			$n_f^* = 50$	
$\mathcal{L}_{\text{div}}$	Dense	Sparse	Finet.	Sparse	Finet.	Dense	Sparse	Finet.	Sparse	Finet.	Dense	Sparse	Finet.	Sparse	Finet.	Dense	Sparse	Finet.	Sparse	Finet.
✗	**86.6** ±0.4	81.8 ±0.3	85.3 ±0.2	79.5 ±0.3	83.4 ±0.2	90.0 ±0.3	88.4 ±0.3	89.4 ±0.2	87.3 ±0.4	88.1 ±0.3	84.2 ±0.1	79.5 ±0.3	83.3 ±0.1	77.3 ±0.3	80.7 ±0.2	93.2 ±0.1	90.9 ±0.2	92.6 ±0.1	89.3 ±0.3	91.1 ±0.1
✓	**86.6** ±0.2	**84.0** ±0.2	**86.5** ±0.1	**81.7** ±0.2	**84.0** ±0.3	**91.4** ±0.2	**90.7** ±0.3	**91.1** ±0.2	**89.8** ±0.4	**90.1** ±0.1	**84.4** ±0.2	**81.0** ±0.2	**84.0** ±0.0	**79.8** ±0.2	**81.7** ±0.1	**93.6** ±0.2	**92.1** ±0.3	**93.3** ±0.1	**91.1** ±0.1	**92.0** ±0.2

Table 7: Accuracy in percent dependent on $\mathcal{L}_{\text{div}}$ for Resnet50. Best results per column are in bold and $\pm$ indicates the standard deviation across five runs.

	CUB-2011					FGVC-Aircraft					NABirds					Stanford Cars				
		$n_f^* = n_f$		$n_f^* = 50$			$n_f^* = n_f$		$n_f^* = 50$			$n_f^* = n_f$		$n_f^* = 50$			$n_f^* = n_f$		$n_f^* = 50$	
Backbone	Dense	Sparse	Finet.	Sparse	Finet.	Dense	Sparse	Finet.	Sparse	Finet.	Dense	Sparse	Finet.	Sparse	Finet.	Dense	Sparse	Finet.	Sparse	Finet.
DenseNet121	86.3 ±0.0	76.2 ±0.5	82.9 ±0.5	75.7 ±0.7	83.1 ±0.1	**91.5** ±0.1	88.2 ±0.5	89.8 ±0.4	88.1 ±0.2	90.0 ±0.4	84.1 ±0.1	72.8 ±0.4	64.6 ±22.8	71.0 ±0.5	80.5 ±0.3	93.3 ±0.1	87.3 ±0.4	91.7 ±0.1	85.8 ±0.3	91.4 ±0.2
Inception-v3	82.3 ±0.1	78.0 ±0.3	80.3 ±0.4	74.0 ±0.7	78.3 ±0.4	88.9 ±0.1	87.5 ±0.2	88.1 ±0.2	85.9 ±0.3	87.4 ±0.2	79.0 ±0.1	75.8 ±0.2	77.3 ±0.3	73.1 ±0.2	76.5 ±0.1	91.5 ±0.1	88.9 ±0.2	90.3 ±0.2	86.3 ±0.2	89.4 ±0.2
Resnet50	**86.6** ±0.2	**84.0** ±0.2	**86.5** ±0.1	**81.7** ±0.2	**84.0** ±0.3	91.4 ±0.2	**90.7** ±0.3	**91.1** ±0.2	**89.8** ±0.4	**90.1** ±0.1	**84.4** ±0.2	**81.0** ±0.2	**84.0** ±0.0	**79.8** ±0.2	**81.7** ±0.1	**93.6** ±0.2	**92.1** ±0.3	**93.3** ±0.1	**91.1** ±0.1	**92.0** ±0.2

Table 8: Accuracy in percent dependent on backbone. Best results per column are in bold and $\pm$ indicates the standard deviation across five runs.

A Appendix

In this appendix, we provide implementation details and standard deviations for the experiments. Additionally, the pseudocode for *glm-saga (Wong et al., 2021)* is shown. Finally, we present the feature visualization technique and more ablations on $\mathcal{L}_{\text{div}}$.

B Detailed Results

The full results of Section 4.2 with the standard deviations are presented in Tables 7 to 13. The reported standard deviations are, except for DenseNet121 on NABirds, as mentioned in Section 4.2, generally rather small compared to the differences in means, which supports our conclusions. We also show exemplary images with the 5 most important features for the dense and sparse conventional model in Figures 9 to 17. The comparison with the finetuned *SLDD-Model* shows an improved localization and interpretability of the features. The finetuned *SLDD-Model* in Figure 10 seems to use features that each individually focus more on chest, lower belly, head, bill or crown, whereas for the dense and sparse models the different features focus on the same regions. This increased diversity@5 and with it interpretability was also measured in Section 4.2.

B.1 Implementation Details

We use Pytorch (Paszke et al., 2019) to implement our methods and on ImageNet pretrained models as backbone feature extractor. We utilized *glm-saga* and *robustness* (Engstrom et al., 2019). The images are resized to 448×448 (299×299 for Inception-v3, 224×224 for ImageNet-1K), normalized, randomly horizontally flipped and jitter is applied. The model is finetuned using stochastic gradient descent on the specific dataset for 150 (100 for NABirds) epochs with a batch size of 16 (64 for ImageNet-1K), starting with $5 \cdot 10^{-3}$ as learning rate for the pretrained layer and 0.01 for the final linear layer. Both get multiplied by 0.4 every 30 epochs. Additionally, we used momentum of 0.9, ℓ_2-regularization of $5 \cdot 10^{-4}$ and apply a dropout rate of 0.2 on the features to reduce dependencies. β was set to 0.196 for Resnet50, 0.098 for DenseNet121 and 0.049 for Inception-v3. For the feature selection, we set $\alpha = 0.8$ and reduce the regularization strength λ by $90\,\%$ as we found it sped up the process without decreasing performance.
We use *glm-saga* to compute the regularization path with $\alpha = 0.99$ and all other parameters set to default with a lookbehind of $T = 5$. From this path, the solution with maximum $n_{wc} \leq 10$ is selected. Then the non-zero

ImageNet-1K				
	$n_f^* = 2048$		$n_f^* = 50$	
Dense	Sparse	Finet.	Sparse	Finet.
80.9	62.2 ±0.0	76.7 ±0.0	44.8 ±0.1	72.8 ±0.1

Table 9: Accuracy in percent for Resnet50 on ImageNet-1Kusing the pretrained dense model.. Best results per column are in bold and $\pm$ indicates the standard deviation across four runs.

Algorithm 1 Pseudocode from *glm-saga (Wong et al., 2021)*

Initialize table of scalars $a'_i = 0$ for $i \in [n]$
Initialize average gradient of table $g_{avg} = 0$ and $g_{0avg} = 0$
for minibatch $B \subset [n]$ **do**
  for $i \in B$ **do**
    $a_i = x_i^T \beta + \beta_0 - y_i$
    $g_i = a_i \cdot x_i$ *// calculate new gradient information*
    $g'_i = a'_i \cdot x_i$ *// calculate stored gradient information*
  end for
  $g = \frac{1}{|B|} \sum_{i \in B} g_i$
  $g' = \frac{1}{|B|} \sum_{i \in B} g'_i$
  $g_0 = \frac{1}{|B|} \sum_{i \in B} a_i$
  $g'_0 = \frac{1}{|B|} \sum_{i \in B} a'_i$
  $\beta = \beta - \gamma(g - g' + g_{avg})$
  $\beta_0 = \beta_0 - \gamma(g_0 - g'_0 + g_{0avg})$
  $\beta = \text{Prox}_{\gamma\lambda\alpha, \gamma\lambda(1-\alpha)}(\beta)$
  for $i \in B$ **do**
    $a'_i = a_i$ *// update table*
    $g_{avg} = g_{avg} + \frac{|B|}{n}(g - g')$ *// update average*
    $g_{0avg} = g_{0avg} + \frac{|B|}{n}(g_0 - g'_0)$
  end for
end for

entries with the lowest absolute value get zeroed out until we are left with $n_{wc} = 5$, as we empirically found that they do not improve test accuracy after finetuning.
This selected solution replaces the final layer of our model. Then we train for 40 epochs, starting with the final learning rate of the initial training multiplied by 100 ($\frac{1}{100}$ of that for ImageNet-1K), and decrease it by $60\,\%$ every 10 epochs. Dropout on the features was set to 0.1 and momentum was increased to 0.95. Note that, while the increased momentum has been important for the stability of the final training, the hyperparameters were not thoroughly optimized for the sparse case.

B.1.1 Competitors

For creating the accuracy for Resnet50 and *CBM (Koh et al., 2020) - joint* in Table 2 we resized the images to 448×448 and used a batch size of 16. The remaining used hyperparameters were almost identical to the *CBM* experiments with Inception-v3, but we only trained for up to 400 epochs, as 650 led to decreased accuracy (-0.8 percent points). Additionally, the learning rate was not decayed, mirroring the published code. The reported accuracy stems from three runs with a standard deviation of 0.7.
For MCL, we used the reported hyperparameters of $\mu = 0.005$ and $\lambda = 10$. For finetuning, we assigned every feature to every class that was using it. We optimized the hyperparameters for FRL based on accuracy, leading to $K = 10$ and $\lambda = 0.01$.

C *Glm-saga*

This section includes the Pseudocode for *glm-saga (Wong et al., 2021)* in algorithm 1. The proximal operator $\text{Prox}_{\lambda_1, \lambda_2}(\beta)$ is defined as:

$$\text{Prox}_{\lambda_1, \lambda_2}(\beta) = \begin{cases} \frac{\beta - \lambda_1}{1 + \lambda_2} & \text{if } \beta > \lambda_1 \\ \frac{\beta + \lambda_1}{1 + \lambda_2} & \text{if } \beta < \lambda_1 \\ 0 & \text{otherwise} \end{cases} \tag{8}$$

D Visualization of Features

For feature visualization, we follow a masking approach. We systematically blur, following (Fong and Vedaldi, 2017), one patch of size $p \times p$ of the image and measure the difference in feature activation between the augmented image and not augmented image. The actual localization map $\boldsymbol{L}_p \in \mathbb{R}^{n_f^* \times \frac{w}{p} \times \frac{h}{p}}$ for that square size

	CUB-2011					FGVC-Aircraft					NABirds					Stanford Cars				
	$n_f^* = 2048$			$n_f^* = 50$		$n_f^* = 2048$			$n_f^* = 50$		$n_f^* = 2048$			$n_f^* = 50$		$n_f^* = 2048$			$n_f^* = 50$	
$\mathcal{L}_{\text{div}}$	Dense	Sparse	Finet.	Sparse	Finet.	Dense	Sparse	Finet.	Sparse	Finet.	Dense	Sparse	Finet.	Sparse	Finet.	Dense	Sparse	Finet.	Sparse	Finet.
✗	50.2 ±0.2	46.0 ±0.2	43.4 ±0.3	48.0 ±0.5	46.5 ±0.3	46.5 ±0.5	43.8 ±0.7	40.9 ±0.4	45.9 ±0.6	44.0 ±0.6	41.5 ±0.2	38.4 ±0.1	34.9 ±0.1	40.8 ±0.6	35.1 ±0.7	45.0 ±0.2	41.7 ±0.3	39.1 ±0.1	43.6 ±0.6	43.7 ±0.4
✓	**98.9** ±0.1	**69.9** ±0.5	**71.9** ±0.4	**65.2** ±1.4	**72.6** ±0.3	**98.8** ±0.2	**85.7** ±1.5	**86.6** ±1.4	**69.3** ±0.8	**73.9** ±1.3	**98.7** ±0.1	**69.5** ±1.1	**81.0** ±1.2	**70.7** ±1.9	**85.3** ±1.0	**99.2** ±0.1	**72.4** ±2.0	**74.6** ±1.5	**63.7** ±1.3	**74.8** ±0.9

Table 10: diversity@5 in percent dependent on $\mathcal{L}_{\text{div}}$ for Resnet50. Best results per column are in bold and $\pm$ indicates the standard deviation across five runs.

	CUB-2011					FGVC-Aircraft					NABirds					Stanford Cars				
	$n_f^* = n_f$			$n_f^* = 50$		$n_f^* = n_f$			$n_f^* = 50$		$n_f^* = n_f$			$n_f^* = 50$		$n_f^* = n_f$			$n_f^* = 50$	
Backbone	Dense	Sparse	Finet.	Sparse	Finet.	Dense	Sparse	Finet.	Sparse	Finet.	Dense	Sparse	Finet.	Sparse	Finet.	Dense	Sparse	Finet.	Sparse	Finet.
DenseNet121	98.5 ±0.1	69.1 ±1.7	64.2 ±1.2	**76.2** ±1.0	71.2 ±0.8	**99.0** ±0.1	40.4 ±0.7	39.9 ±0.9	64.3 ±2.0	62.6 ±2.1	98.6 ±0.1	45.7 ±1.1	42.3 ±3.5	63.1 ±3.1	66.2 ±2.2	98.7 ±0.1	47.4 ±1.3	46.3 ±1.0	**71.8** ±1.5	68.0 ±1.2
Inception-v3	86.3 ±0.5	**74.9** ±0.9	65.1 ±0.6	53.2 ±0.8	52.7 ±0.4	95.1 ±0.2	**87.2** ±1.6	72.2 ±1.4	53.7 ±1.1	56.1 ±0.9	81.8 ±1.0	47.9 ±1.0	47.0 ±0.8	42.7 ±1.6	45.6 ±1.0	92.0 ±0.3	**76.3** ±0.6	63.7 ±0.6	52.0 ±1.2	50.7 ±0.8
Resnet50	**98.9** ±0.1	69.9 ±0.5	**71.9** ±0.4	65.2 ±1.4	**72.6** ±0.3	98.8 ±0.2	85.7 ±1.5	**86.6** ±1.4	**69.3** ±0.8	**73.9** ±1.3	**98.7** ±0.1	**69.5** ±1.1	**81.0** ±1.2	**70.7** ±1.9	**85.3** ±1.0	**99.2** ±0.1	72.4 ±2.0	**74.6** ±1.5	63.7 ±1.3	**74.8** ±0.9

Table 11: diversity@5 in percent dependent on backbone. Best results per column are in bold and $\pm$ indicates the standard deviation across five runs.

is computed by

$$\boldsymbol{L}_{pxy} = \text{ReLU}(\boldsymbol{f}(I) - \boldsymbol{f}(I_{pxy})) \tag{9}$$

where I_{pxy} indicates the image where a p-sized patch starting at position $(x * p, y * p)$ is blurred and the ReLU suppresses parts that increased the feature activation, since blur should not be injecting a feature. The final localization map is the combination of different square sizes $p \in \{28, 56, 64, 112, 224\}$ to accommodate for differently sized features:

$$\boldsymbol{L} = \sum_p \frac{\boldsymbol{L}_p}{\max(\boldsymbol{L}_p)} \tag{10}$$

Notably, $\boldsymbol{L}_p$ has to be resized according to the smallest p and we only show $\boldsymbol{L}^i$ for one feature i.

E Feature Alignment

In this section, we use the alignment of the shown feature in Figure 4b with four-engine aircraft to exemplary show how one can align a feature manually. We first visualize the distribution of the feature over the training data in Figure 6. This indicates a more binary attribute and by investigating the images and saliency maps, we observed an alignment with four-engine aircraft. We test the hypothesis by filtering for the classes "A340-500" and "BAE 146-300", for which the feature corresponds to the four engines. Figure 7 shows that the lowest activating examples of this group do not clearly show the four-engines which supports our hypothesis. Note that one feature can correspond to multiple concepts, as another hypothesis is an alignment with the propeller. Whether all correlating concepts have to be understood or how exact the analysis has to be depends on the application.

F Ablations on Feature Diversity Loss

In this section, we present an additional analysis of the factors in $\mathcal{L}_{\text{div}}$ and the impact of β.

	CUB-2011					FGVC-Aircraft					Stanford Cars				
	$n_f^* = 2048$			$n_f^* = 50$		$n_f^* = 2048$			$n_f^* = 50$		$n_f^* = 2048$			$n_f^* = 50$	
$\mathcal{L}_{\text{div}}$	Dense	Sparse	Finet.	Sparse	Finet.	Dense	Sparse	Finet.	Sparse	Finet.	Dense	Sparse	Finet.	Sparse	Finet.
✗	**86.6** ±0.4	81.8 ±0.3	85.3 ±0.2	79.5 ±0.3	83.4 ±0.2	90.0 ±0.3	88.4 ±0.3	89.4 ±0.2	87.3 ±0.4	88.1 ±0.3	93.2 ±0.1	90.9 ±0.2	92.6 ±0.1	89.3 ±0.3	91.1 ±0.1
✓	**86.6** ±0.2	**84.0** ±0.2	**86.5** ±0.1	**81.7** ±0.2	**84.0** ±0.3	**91.4** ±0.2	**90.7** ±0.3	**91.1** ±0.2	**89.8** ±0.4	**90.1** ±0.1	**93.6** ±0.2	**92.1** ±0.3	**93.3** ±0.1	**91.1** ±0.1	**92.0** ±0.2
MCL (Chang et al., 2020)	86.1 ±0.2	81.9 ±0.3	85.1 ±0.2	79.4 ±0.2	82.8 ±0.1	90.1 ±0.1	88.4 ±0.2	89.0 ±0.2	87.2 ±0.5	88.1 ±0.1	93.1 ±0.1	91.0 ±0.2	92.5 ±0.2	89.0 ±0.5	90.7 ±0.3
FRL (Zheng et al., 2020)	86.4 ±0.2	81.5 ±0.2	85.3 ±0.2	78.9 ±0.5	82.6 ±0.5	90.0 ±0.1	88.5 ±0.2	89.4 ±0.4	87.5 ±0.2	88.2 ±0.2	93.3 ±0.1	90.8 ±0.3	92.6 ±0.2	89.4 ±0.2	90.9 ±0.2

Table 12: Accuracy in percent for Resnet50 compared to other loss functions. Best results per column are in bold and $\pm$ indicates the standard deviation across five runs.

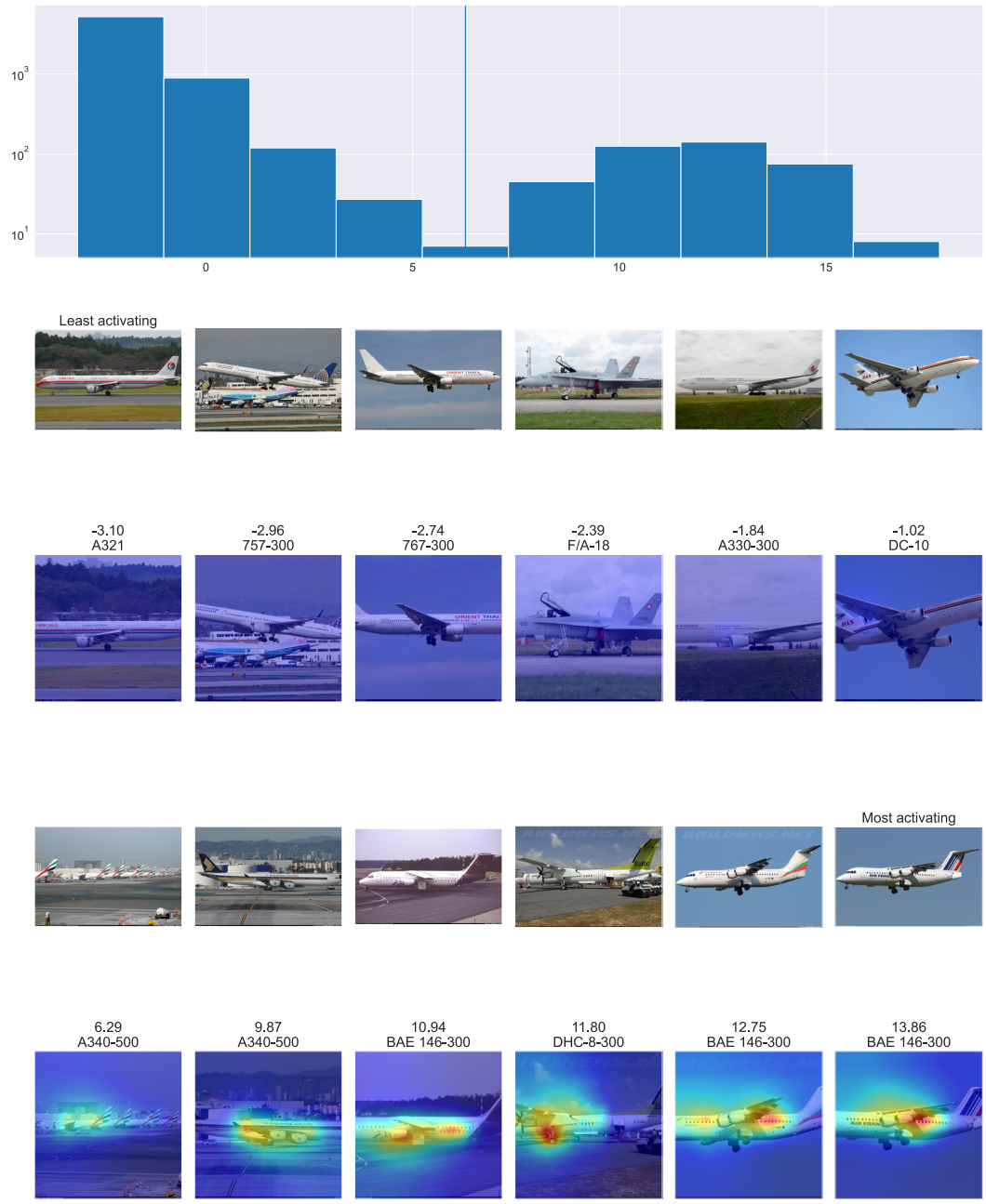

Figure 6: Top: Distribution of feature activation over the training data. Bottom: Different examples of this distribution with their scaled feature localization. The activation and class name is given above the image.

F.1 Factor Importance

We analyzed the impact of the two factors in Equation 3 with for accuracy optimized β, shown in Tables 14 and 15. The label *w/o Class-Specific* indicates not using the weights of the predicted class and *w/o Rescaling* refers to not maintaining their relative mean. We used $\beta = 0.001 \cdot \frac{196}{2048} \approx 1\text{e}{-5}$ for *w/o Class-Specific*, since we use the size of the feature maps with $196 = w_M \cdot h_M$ and the number of features of the baseline model $n_f = 2048$ as scaling factors in order to be less dependent of model architecture and image size, and $\beta = 0.1$ for *w/o Rescaling*. Only the combination of both factors leads to an improved accuracy, validating our idea that it is important to only enforce diversity of features that are found in the input and used in conjunction.

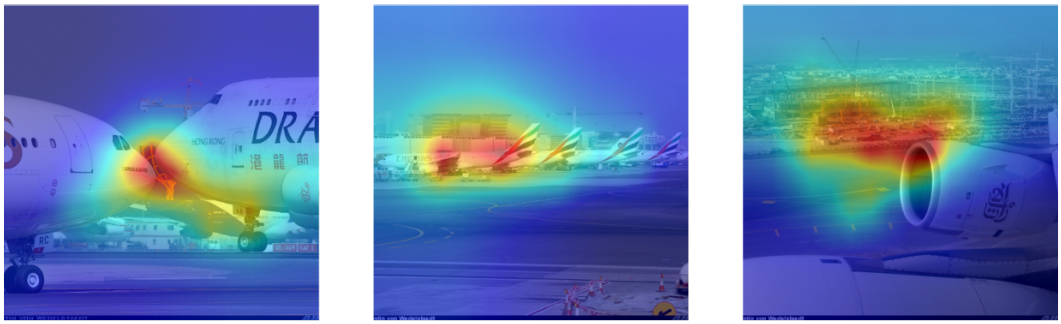

Figure 7: The three least activating training examples of classes "A340-500" and "BAE-16-300" for the given feature.

$\mathcal{L}_{\text{div}}$	CUB-2011 $n_f^*=2048$ Dense	CUB-2011 $n_f^*=2048$ Sparse	CUB-2011 $n_f^*=2048$ Finet.	CUB-2011 $n_f^*=50$ Sparse	CUB-2011 $n_f^*=50$ Finet.	FGVC-Aircraft $n_f^*=2048$ Dense	FGVC-Aircraft $n_f^*=2048$ Sparse	FGVC-Aircraft $n_f^*=2048$ Finet.	FGVC-Aircraft $n_f^*=50$ Sparse	FGVC-Aircraft $n_f^*=50$ Finet.	Stanford Cars $n_f^*=2048$ Dense	Stanford Cars $n_f^*=2048$ Sparse	Stanford Cars $n_f^*=2048$ Finet.	Stanford Cars $n_f^*=50$ Sparse	Stanford Cars $n_f^*=50$ Finet.
✗	50.2 ±0.2	46.0 ±0.2	43.4 ±0.3	48.0 ±0.5	46.5 ±0.3	46.5 ±0.5	43.8 ±0.7	40.9 ±0.4	45.9 ±0.6	44.0 ±0.6	45.0 ±0.2	41.7 ±0.3	39.1 ±0.1	43.6 ±0.6	43.7 ±0.4
✓	**98.9** ±0.1	**69.9** ±0.5	**71.9** ±0.4	**65.2** ±1.4	**72.6** ±0.3	**98.8** ±0.2	**85.7** ±1.5	**86.6** ±1.4	**69.3** ±0.8	**73.9** ±1.3	**99.2** ±0.1	**72.4** ±2.0	**74.6** ±1.5	**63.7** ±1.3	**74.8** ±0.9
MCL (Chang et al., 2020)	52.5 ±0.3	51.4 ±0.7	48.9 ±0.8	56.7 ±1.0	52.3 ±1.0	50.1 ±0.7	50.6 ±0.8	48.3 ±1.2	51.7 ±1.8	50.1 ±1.9	49.0 ±0.6	49.0 ±0.9	46.2 ±0.8	51.8 ±1.2	49.5 ±1.3
FRL (Zheng et al., 2020)	51.1 ±0.3	47.1 ±0.5	44.1 ±0.4	49.0 ±0.7	46.3 ±0.6	48.2 ±0.3	44.6 ±0.3	41.2 ±0.4	44.9 ±0.8	43.1 ±0.5	46.2 ±0.1	43.0 ±0.4	40.0 ±0.4	43.0 ±1.1	41.7 ±1.1

Table 13: diversity@5 in percent for Resnet50 compared to other loss functions. Best results per column are in bold and $\pm$ indicates the standard deviation across five runs.

Loss	CUB-2011 $n_f^*=2048$ Dense	CUB-2011 $n_f^*=2048$ Sparse	CUB-2011 $n_f^*=2048$ Finet.	CUB-2011 $n_f^*=50$ Sparse	CUB-2011 $n_f^*=50$ Finet.	FGVC-Aircraft $n_f^*=2048$ Dense	FGVC-Aircraft $n_f^*=2048$ Sparse	FGVC-Aircraft $n_f^*=2048$ Finet.	FGVC-Aircraft $n_f^*=50$ Sparse	FGVC-Aircraft $n_f^*=50$ Finet.	Stanford Cars $n_f^*=2048$ Dense	Stanford Cars $n_f^*=2048$ Sparse	Stanford Cars $n_f^*=2048$ Finet.	Stanford Cars $n_f^*=50$ Sparse	Stanford Cars $n_f^*=50$ Finet.
$\mathcal{L}_{\text{div}}$	**86.6** ±0.2	**84.0** ±0.2	**86.5** ±0.1	**81.7** ±0.2	**84.0** ±0.3	**91.4** ±0.2	**90.7** ±0.3	**91.1** ±0.2	**89.8** ±0.4	**90.1** ±0.1	**93.6** ±0.2	**92.1** ±0.3	**93.3** ±0.1	**91.1** ±0.1	**92.0** ±0.2
w/o Rescaling	86.3 ±0.2	82.7 ±0.4	85.6 ±0.3	80.2 ±0.5	83.4 ±0.3	90.8 ±0.4	89.7 ±0.3	90.1 ±0.2	88.7 ±0.4	89.1 ±0.3	93.2 ±0.1	91.0 ±0.2	92.8 ±0.2	89.9 ±0.1	91.5 ±0.2
w/o Class-Specific	86.3 ±0.2	82.0 ±0.2	85.4 ±0.3	79.0 ±0.2	83.1 ±0.2	90.2 ±0.3	88.6 ±0.4	89.6 ±0.3	87.3 ±0.2	88.5 ±0.4	93.2 ±0.2	90.8 ±0.2	92.6 ±0.2	89.1 ±0.3	91.0 ±0.3

Table 14: Impact of factors in $\mathcal{L}_{\text{div}}$ on accuracy in percent for Resnet50. Best results per column are in bold and $\pm$ indicates the standard deviation across five runs.

Loss	CUB-2011 $n_f^*=2048$ Dense	CUB-2011 $n_f^*=2048$ Sparse	CUB-2011 $n_f^*=2048$ Finet.	CUB-2011 $n_f^*=50$ Sparse	CUB-2011 $n_f^*=50$ Finet.	FGVC-Aircraft $n_f^*=2048$ Dense	FGVC-Aircraft $n_f^*=2048$ Sparse	FGVC-Aircraft $n_f^*=2048$ Finet.	FGVC-Aircraft $n_f^*=50$ Sparse	FGVC-Aircraft $n_f^*=50$ Finet.	Stanford Cars $n_f^*=2048$ Dense	Stanford Cars $n_f^*=2048$ Sparse	Stanford Cars $n_f^*=2048$ Finet.	Stanford Cars $n_f^*=50$ Sparse	Stanford Cars $n_f^*=50$ Finet.
$\mathcal{L}_{\text{div}}$	98.9 ±0.1	**69.9** ±0.5	**71.9** ±0.4	65.2 ±1.4	72.6 ±0.3	98.8 ±0.2	**85.7** ±1.5	**86.6** ±1.4	**69.3** ±0.8	**73.9** ±1.3	99.2 ±0.1	**72.4** ±2.0	**74.6** ±1.5	63.7 ±1.3	**74.8** ±0.9
w/o Rescaling	**99.3** ±0.0	67.6 ±0.9	66.9 ±0.5	**70.5** ±2.0	**73.3** ±1.8	**99.7** ±0.0	72.4 ±1.2	74.6 ±1.6	68.5 ±4.3	73.6 ±2.1	**99.7** ±0.0	64.9 ±0.8	65.3 ±0.6	**68.3** ±3.6	73.5 ±2.0
w/o Class-Specific	50.6 ±0.3	46.2 ±0.3	43.5 ±0.2	48.1 ±1.1	46.8 ±0.6	47.6 ±0.6	44.3 ±0.5	41.2 ±0.3	45.0 ±1.7	43.7 ±1.6	45.5 ±0.2	42.2 ±0.3	39.5 ±0.2	42.7 ±1.1	42.5 ±1.1

Table 15: Impact of factors in $\mathcal{L}_{\text{div}}$ on diversity@5 in percent for Resnet50. Best results per column are in bold and $\pm$ indicates the standard deviation across five runs.

	CUB-2011					FGVC-Aircraft					Stanford Cars				
	$n_f^*=2048$			$n_f^*=50$		$n_f^*=2048$			$n_f^*=50$		$n_f^*=2048$			$n_f^*=50$	
β	Dense	Sparse	Finet.	Sparse	Finet.	Dense	Sparse	Finet.	Sparse	Finet.	Dense	Sparse	Finet.	Sparse	Finet.
0	**86.6** ±0.4	81.8 ±0.3	85.3 ±0.2	79.5 ±0.3	83.4 ±0.2	90.0 ±0.3	88.4 ±0.3	89.4 ±0.2	87.3 ±0.4	88.1 ±0.3	93.2 ±0.1	90.9 ±0.2	92.6 ±0.1	89.3 ±0.3	91.1 ±0.1
0.00196	86.4 ±0.2	82.0 ±0.3	85.5 ±0.3	79.3 ±0.3	83.3 ±0.2	90.2 ±0.2	88.7 ±0.3	89.5 ±0.3	87.6 ±0.2	88.5 ±0.2	93.1 ±0.1	90.9 ±0.3	92.6 ±0.1	89.0 ±0.2	90.8 ±0.2
0.0196	86.4 ±0.2	82.2 ±0.3	85.3 ±0.3	79.4 ±0.6	83.2 ±0.3	90.6 ±0.4	89.0 ±0.3	89.7 ±0.3	87.4 ±0.4	88.5 ±0.4	93.1 ±0.1	91.0 ±0.2	92.6 ±0.2	89.0 ±0.2	90.9 ±0.2
<u>0.196</u>	**86.6** ±0.2	**84.0** ±0.2	**86.5** ±0.1	**81.7** ±0.2	**84.0** ±0.3	**91.4** ±0.2	**90.7** ±0.3	**91.1** ±0.2	**89.8** ±0.4	**90.1** ±0.1	**93.6** ±0.2	**92.1** ±0.3	**93.3** ±0.1	**91.1** ±0.1	**92.0** ±0.2

Table 16: Accuracy in percent dependent on β for Resnet50. Best results per column are in bold and $\pm$ indicates the standard deviation across five runs. Our used β is underlined.

	CUB-2011					FGVC-Aircraft					Stanford Cars				
	$n_f^*=2048$			$n_f^*=50$		$n_f^*=2048$			$n_f^*=50$		$n_f^*=2048$			$n_f^*=50$	
β	Dense	Sparse	Finet.	Sparse	Finet.	Dense	Sparse	Finet.	Sparse	Finet.	Dense	Sparse	Finet.	Sparse	Finet.
0	50.2 ±0.2	46.0 ±0.2	43.4 ±0.3	48.0 ±0.5	46.5 ±0.3	46.5 ±0.5	43.8 ±0.7	40.9 ±0.4	45.9 ±0.6	44.0 ±0.6	45.0 ±0.2	41.7 ±0.3	39.1 ±0.1	43.6 ±0.6	43.7 ±0.4
0.00196	51.0 ±0.1	46.1 ±0.2	43.7 ±0.2	49.2 ±0.6	47.6 ±0.4	48.1 ±0.4	44.6 ±0.4	41.5 ±0.4	45.6 ±0.5	43.8 ±0.3	46.3 ±0.0	42.6 ±0.3	39.7 ±0.2	43.0 ±0.7	43.3 ±0.5
0.0196	64.0 ±0.6	50.8 ±0.6	47.8 ±0.4	50.2 ±1.0	48.6 ±0.9	75.4 ±0.5	54.4 ±0.7	50.2 ±0.6	50.2 ±1.9	48.5 ±1.0	66.1 ±0.7	48.7 ±0.6	45.2 ±0.4	46.6 ±2.0	46.0 ±1.3
<u>0.196</u>	**98.9** ±0.1	**69.9** ±0.5	**71.9** ±0.4	**65.2** ±1.4	**72.6** ±0.3	**98.8** ±0.2	**85.7** ±1.5	**86.6** ±1.4	**69.3** ±0.8	**73.9** ±1.3	**99.2** ±0.1	**72.4** ±2.0	**74.6** ±1.5	**63.7** ±1.3	**74.8** ±0.9

Table 17: diversity@5 in percent dependent on β for Resnet50. Best results per column are in bold and $\pm$ indicates the standard deviation across five runs. Our used β is underlined.

F.2 Loss Weighting

This section is concerned with the impact of the weighting factor β for the feature diversity loss $\mathcal{L}_{\text{div}}$. For our proposed method, we use $\beta = 0.196$. Tables 16 and 17 show that $\mathcal{L}_{\text{div}}$ improves the diversity@5 and accuracy across all datasets in the sparse case with increasing β up to a maximum roughly around $\beta = 1$. Setting the value higher leads to $\mathcal{L}_{\text{div}}$ dominating the training. To ensure that the network is still mainly optimized for classification, we choose $\beta = 0.196$, even though in some cases we could still observe a slight gain in accuracy with a slight increase of β. The positive relation between diversity@5 and accuracy, visualized in Figure 8, supports our approach of enforcing varied features for the extremely sparse case.

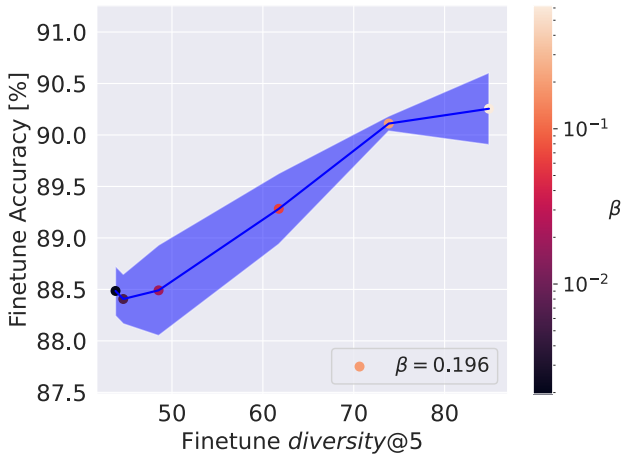

Figure 8: Relationship between finetuned diversity@5 and accuracy for varying β for Resnet50, portrayed via color, on FGVC-Aircraft. Each dot represents an increase by a factor of $\sqrt{10}$ and the standard deviation is indicated by the shaded area. $\beta = 1.96$ $\mathcal{L}_{\text{div}}$ is not shown, as it dominates the training.

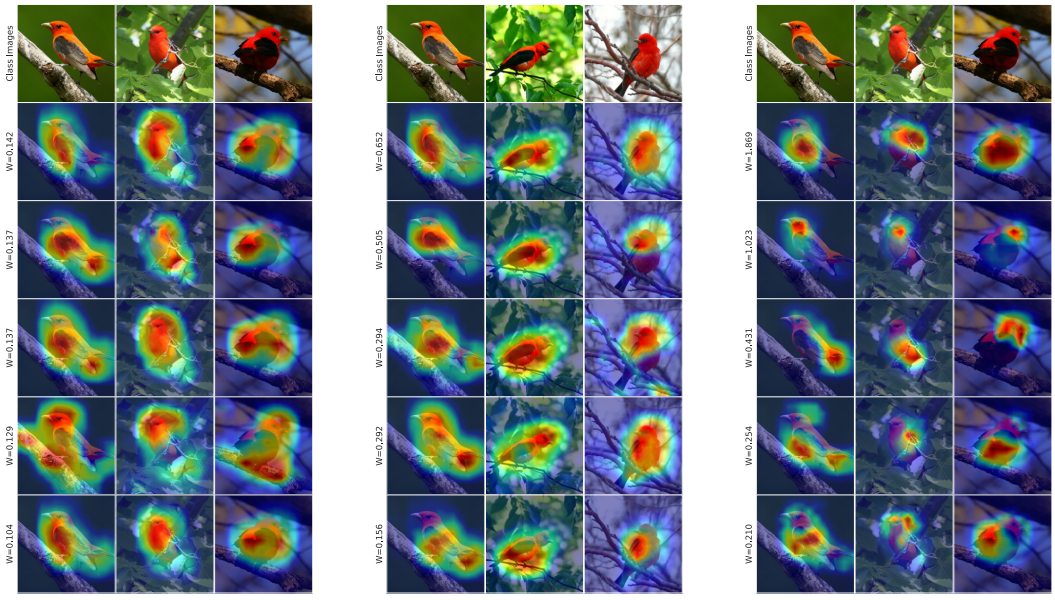

(a) Conventional Dense Model (b) Sparse with $n_f^* = n_f$ (c) Finetuned SLDD-Model

Figure 9: Feature maps of the top 5 features by magnitude for class Scarlet Tanager on example images. The used weights for the respective features are also displayed.

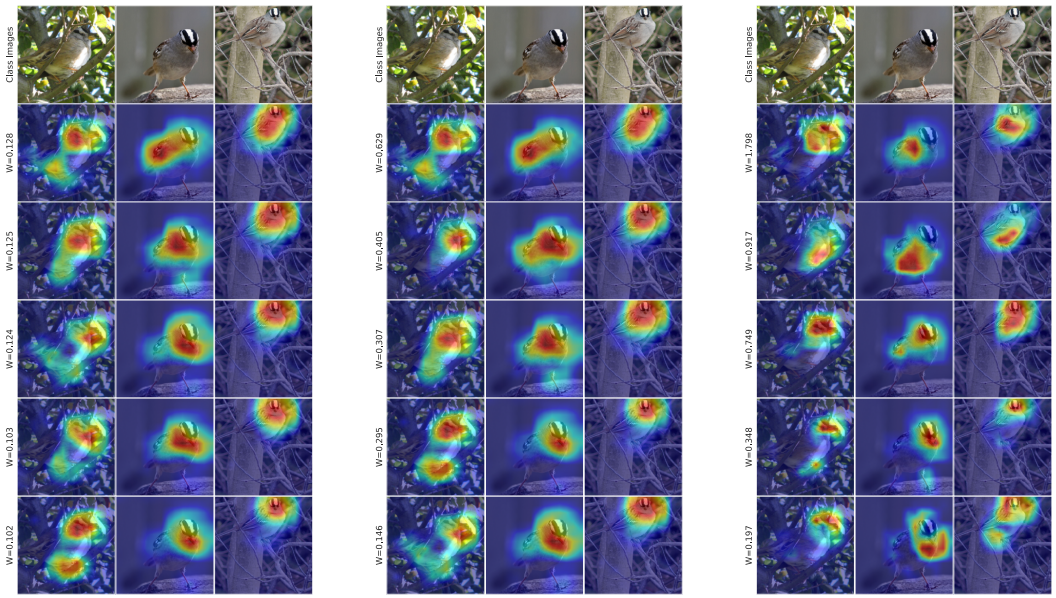

(a) Conventional Dense Model (b) Sparse with $n_f^* = n_f$ (c) Finetuned SLDD-Model

Figure 10: Feature maps of the top 5 features by magnitude for class White Crowned Sparrow on example images. The used weights for the respective features are also displayed.

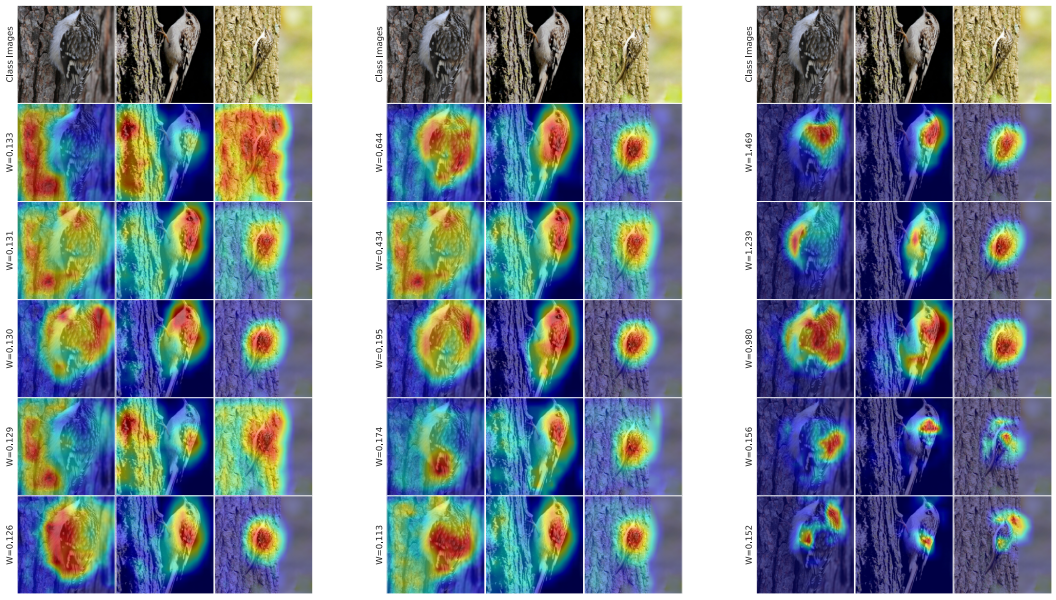

(a) Conventional Dense Model (b) Sparse with $n_f^* = n_f$ (c) Finetuned SLDD-Model

Figure 11: Feature maps of the top 5 features by magnitude for class Brown Creeper on example images. The used weights for the respective features are also displayed.

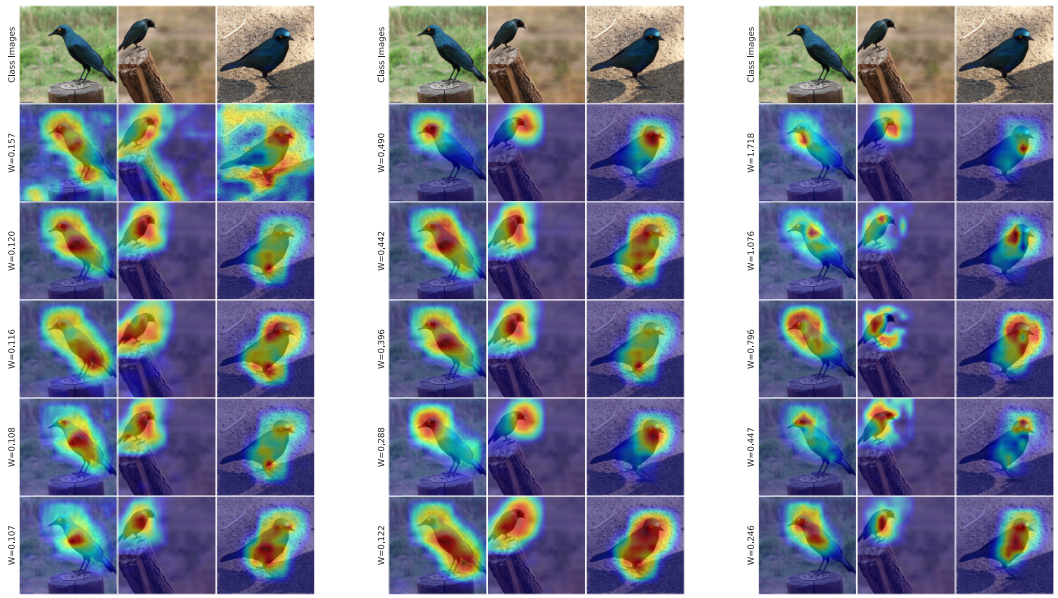

(a) Conventional Dense Model (b) Sparse with $n_f^* = n_f$ (c) Finetuned SLDD-Model

Figure 12: Feature maps of the top 5 features by magnitude for class Cape Glossy Starling on example images. The used weights for the respective features are also displayed.

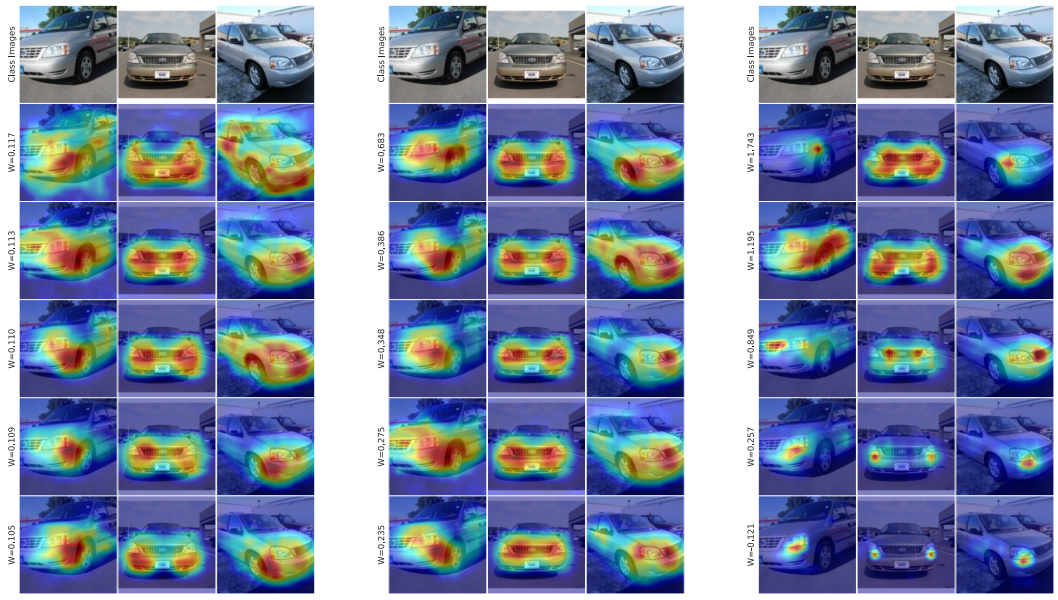

(a) Conventional Dense Model (b) Sparse with $n_f^* = n_f$ (c) Finetuned SLDD-Model

Figure 13: Feature maps of the top 5 features by magnitude for class Ford Freestar Minivan on example images. The used weights for the respective features are also displayed.

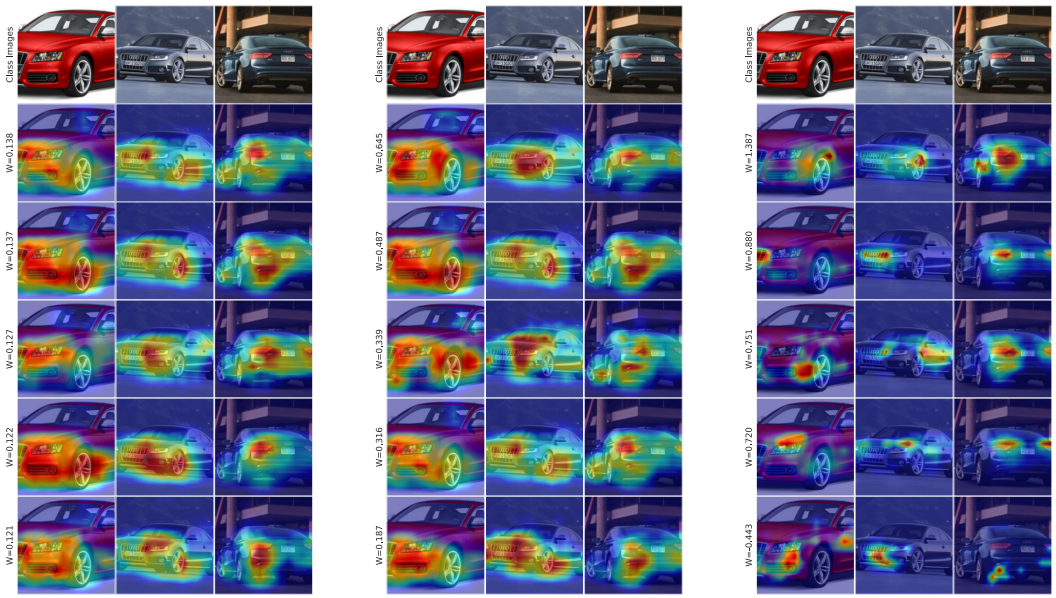

(a) Conventional Dense Model (b) Sparse with $n_f^* = n_f$ (c) Finetuned SLDD-Model

Figure 14: Feature maps of the top 5 features by magnitude for class Audi S5 Coupe 2012 on example images. The used weights for the respective features are also displayed.

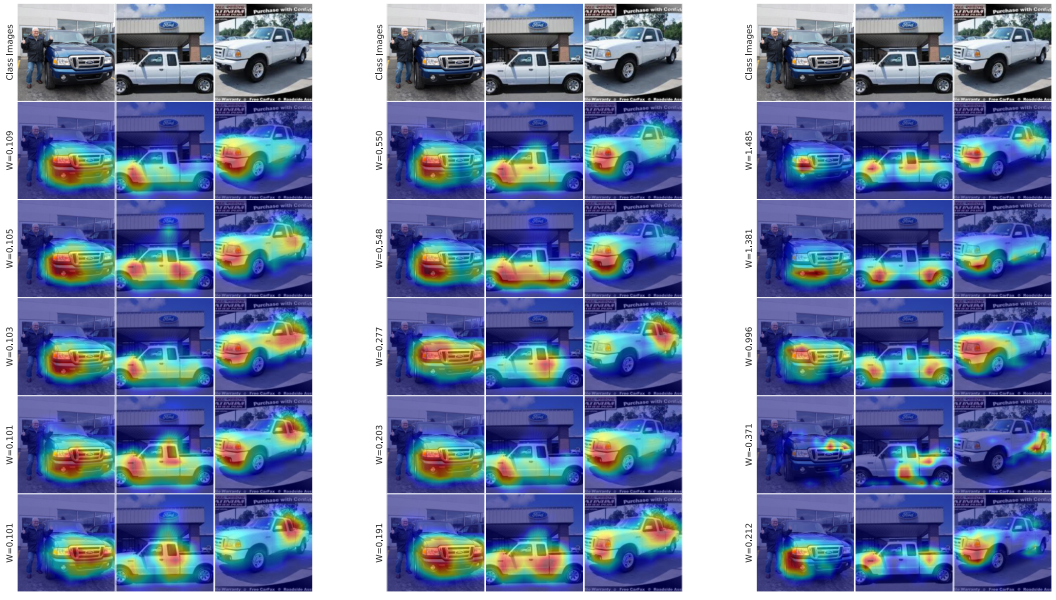

(a) Conventional Dense Model (b) Sparse with $n_f^* = n_f$ (c) Finetuned SLDD-Model

Figure 15: Feature maps of the top 5 features by magnitude for class Ford Ranger SubCab2011 on example images. The used weights for the respective features are also displayed.

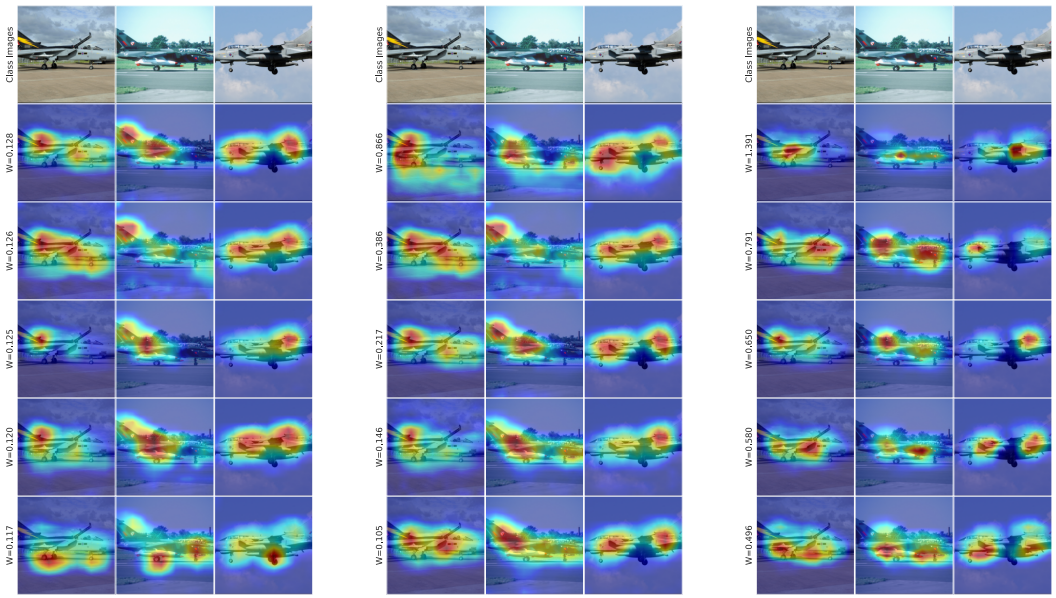

(a) Conventional Dense Model (b) Sparse with $n_f^* = n_f$ (c) Finetuned SLDD-Model

Figure 16: Feature maps of the top 5 features by magnitude for class Tornado on example images. The used weights for the respective features are also displayed.

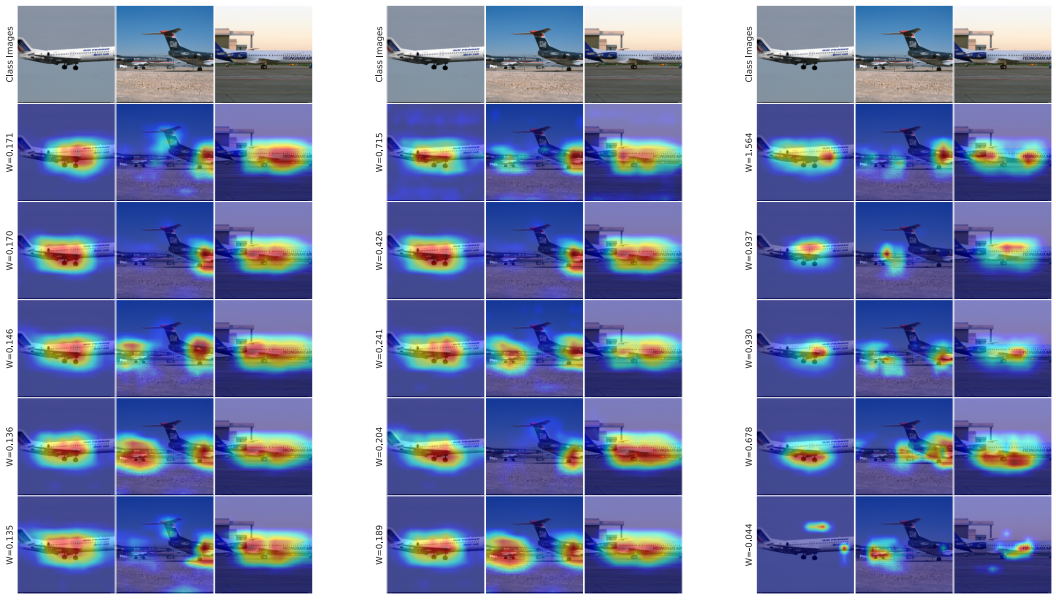

(a) Conventional Dense Model (b) Sparse with $n_f^* = n_f$ (c) Finetuned SLDD-Model

Figure 17: Feature maps of the top 5 features by magnitude for class Fokker 100 on example images. The used weights for the respective features are also displayed.